

# SUPER-EDDINGTON ACCRETION DISKS AROUND SUPERMASSIVE BLACK HOLES

YAN-FEI JIANG(姜燕飞)<sup>1</sup>, JAMES M. STONE<sup>2</sup> & SHANE W. DAVIS<sup>3</sup>

<sup>1</sup>kavli institute for theoretical physics, Kohn Hall, University of California, Santa Barbara 93106, USA

<sup>2</sup>Department of Astrophysical Sciences, Princeton University, Princeton, NJ 08544, USA and

<sup>3</sup>Department of Astronomy, University of Virginia, P.O. Box 400325, Charlottesville, VA 22904-4325, USA

*Draft version April 6, 2024*

## ABSTRACT

We use global three dimensional radiation magneto-hydrodynamical simulations to study accretion disks onto a  $5 \times 10^8 M_\odot$  black hole with accretion rates varying from  $\sim 250 L_{\text{Edd}}/c^2$  to  $1500 L_{\text{Edd}}/c^2$ . We form the disks with torus centered at 50 – 80 gravitational radii with self-consistent turbulence initially generated by the magneto-rotational instability. We study cases with and without net vertical magnetic flux. The inner regions of all disks have radiation pressure  $\sim 10^4 - 10^6$  times the gas pressure. Non-axisymmetric density waves that steepen into spiral shocks form as gas flows towards the black hole. In simulations without net vertical magnetic flux, Reynolds stress generated by the spiral shocks are the dominant mechanism to transfer angular momentum. Maxwell stress from MRI turbulence can be larger than the Reynolds stress only when net vertical magnetic flux is sufficiently large. Outflows are formed with speed  $\sim 0.1 - 0.4c$ . When the accretion rate is smaller than  $\sim 500 L_{\text{Edd}}/c^2$ , outflows start around 10 gravitational radii and the radiative efficiency is  $\sim 5\% - 7\%$  with both magnetic field configurations. With accretion rate reaching  $1500 L_{\text{Edd}}/c^2$ , most of the funnel region close to the rotation axis becomes optically thick and the outflow only develops beyond 50 gravitational radii. The radiative efficiency is reduced to 1%. We always find the kinetic energy luminosity associated with the outflow is only  $\sim 15\% - 30\%$  of the radiative luminosity. The mass flux lost in the outflow is  $\sim 15\% - 50\%$  of the net mass accretion rates. We discuss implications of our simulation results on the observational properties of these disks.

**Keywords:** accretion, accretion disks — (galaxies:) quasars: supermassive black holes — magnetohydrodynamics (MHD) — methods: numerical — radiative transfer

## 1. INTRODUCTION

Active Galactic Nuclei (AGNs) are believed to be powered by accretion of gas onto the central supermassive black hole (SMBH) with black hole mass  $M_{\text{BH}} \sim 10^6 - 10^{10} M_\odot$ . Although the observed bolometric luminosity for most AGNs are estimated to be smaller than the Eddington value  $L_{\text{Edd}} = 4\pi G M_{\text{BH}} c / \kappa_{\text{es}}$  for electron scattering opacity  $\kappa_{\text{es}}$  (e.g. Kollmeier et al. 2006), super-Eddington accretion is expected in many circumstances. For example, narrow-line seyfert 1 galaxies (NLS1) are widely believed to host supermassive black holes with accretion rate close or above the Eddington limit (Pounds et al. 1995; Komossa et al. 2006; Jin et al. 2016, 2017). The weak emission-line quasars have also been suggested to host super-Eddington accretion disks (Luo et al. 2015). The existence of  $\sim 10^9 M_\odot$  black holes around redshift  $z \sim 7$  (Mortlock et al. 2011) implies that super-Eddington accretion around supermassive black holes must happen for at least a fraction of the time in order for these black holes to gain so much mass before this redshift for any reasonable model of black hole seeds (Volonteri et al. 2015; Begelman & Volonteri 2017). Tidal disruption events are also thought to trigger super-Eddington accretions onto supermassive black holes if the stripped mass from the stars can circularize and form an accretion disk efficiently (Rees 1988). Because feedback from AGNs is an important process to regulate the evolution and structures of the host galaxies (e.g., Ciotti & Ostriker 2007; Ciotti et al. 2010; Kormendy & Ho 2013), it is important to understand when and how AGNs can

accrete above the Eddington limit. Although this process may only happen for a small fraction of the duty cycles for AGNs, it can produce significant amount of radiation and outflow from the disks, which may have important feedback effects.

In order to tell whether the disks in AGNs are accreting above the Eddington limit or not, it is useful to predict what to expect from this kind of disks, as direct measurements of black hole mass and bolometric luminosity for AGNs are usually very uncertain. The slim disk model (Abramowicz et al. 1980) is often used to describe accretion disks in this regime and there have been a number of numerical simulations to study the properties of super-Eddington accretion disks recently (Ohsuga et al. 2005; Jiang et al. 2014a; McKinney et al. 2014; Sądowski et al. 2014). However, most of these simulations are designed for stellar mass black holes with electron scattering assumed to be the dominant opacity with a few exceptions (Turner 2004; Jiang et al. 2013b, 2016b). The general hope is that these disks in AGNs are just scaled up versions of disks in X-ray binaries and some of the numerical simulation results are extrapolated to AGN even when they are run with stellar mass black hole parameters. However, although the inner regions of super-Eddington disks for both X-ray binaries and AGNs are radiation pressure dominated, the ratio between radiation pressure and gas pressure is normally smaller than  $\sim 100$  in X-ray binaries while this ratio in AGNs can easily reach  $\sim 10^4 - 10^5$  (Shakura & Sunyaev 1973). The significantly enhanced radiation pressure might affect the properties of disks in many interesting ways that are unique

to AGNs. For example, when the ratio between radiation pressure and gas pressure is larger than the ratio between proton mass and electron mass, bulk comptonization can work efficiently to change the spectra of AGN disks and may explain the soft X-ray excess in AGNs (Socrates et al. 2004; Kaufman et al. 2017). Strongly radiation pressure dominated flow is also well known to be highly compressible (Turner et al. 2003; Jiang et al. 2013b) and radiative damping can significantly change the properties of turbulence generated by magneto-rotational instability (MRI, Balbus & Hawley 1991). Particularly, the ratio between Maxwell stress and total thermal pressure in the strongly radiation pressure dominated compressible flow is usually smaller than the value found by MRI simulations without strong radiation pressure (Jiang et al. 2013b). Finally, the temperature and density regime appropriate for AGN disks, the iron opacity bump changes the structures and stability of AGN disks significantly (Jiang et al. 2016b). These new physical phenomena in the strongly radiation pressure dominated flow suggest that in order to understand the properties of AGN disks, we have to carry out the simulations with realistic parameters to achieve this large ratio between radiation pressure and gas pressure with realistic opacities. The focus of this paper is to show a set of numerical simulations to achieve this goal for the first time.

MRI turbulence is now widely believed to be responsible for the angular momentum transfer in the fully ionized AGN disks. All the previous numerical simulations of AGN disks with self-consistent thermal properties (Turner 2004; Jiang et al. 2016b) are done for local patches of disks under the shearing box approximation to study properties of the saturation state of MRI. Global simulations are necessary to study the radial structures of the disks and outflow, particularly in the super-Eddington regime. Global simulations also allow for other hydrodynamic mechanisms of angular momentum transfer to manifest (Fromang & Lesur 2017), which may not be correctly captured by the local shearing box simulations. One important result of this paper is to show that global coherent spiral density waves can be excited in AGN disks, which may play an important role for angular momentum transfer when the saturation state of MRI turbulence is suppressed by radiative damping. Global simulations are significantly more expensive compared with local shearing box simulations if we want to resolve the accretion disk region while capture the large scale outflow. To achieve this goal, we use the static mesh refinement technique in the recently developed radiation MHD code *Athena++* (Stone et al., in preparation). For the simulations in this paper, we place the initial torus as far as we can from the black hole (typically 80 gravitational radii) and let the disk form from vacuum self-consistently.

Properties of MRI turbulence are well known to depend on the configurations of the initial seed magnetic fields since the first 3D simulation of MRI turbulence done by Hawley et al. (1995). When there are net poloidal magnetic fields through the disk, both local and shearing box simulations show that the ratio between Maxwell stress and thermal pressure is larger compared to the case without net vertical magnetic fields (Bai & Stone 2013; Suzuki & Inutsuka 2014; Salvesen et al. 2016; Zhu & Stone 2017). Particularly, efficiency of radiative damp-

ing on MRI turbulence (Jiang et al. 2013b) may also depend on the amount of poloidal magnetic fields. Our previous simulation for super-Eddington accretion disk of stellar mass black holes (Jiang et al. 2014a) found that magnetic buoyancy caused by MRI turbulence could enhance the advective cooling along the vertical direction of the disk, which increased the radiative efficiency of super-Eddington accretion disks compared to the classical slim disk model. It is also interesting to see how different magnetic field configurations change the importance of this effect.

Because it is very expensive to solve radiative transfer equation directly, flux limited diffusion (FLD) or M1 closure scheme are usually adopted in most of previous numerical simulations of super-Eddington accretion disks (Ohsuga et al. 2005; Sądowski et al. 2014; McKinney et al. 2014). It is usually argued that these approximate numerical schemes should work fine near the optically thick part of the disk, where diffusion approximation should be valid. However, as pointed out by Kaufman et al. (2017), these approximate local closure schemes does not include the second order energy exchange in terms of the ratio between flow velocity and the speed of light, which is essential for radiation viscosity. This effect may be safely neglected when the ratio between radiation and gas pressure is not too large, which is not true for AGN disks. Instead of using these approximate closure scheme, we solve the time dependent radiative transfer equation directly based on the numerical algorithm developed by Jiang et al. (2014a). This allows us to capture the physics of radiation viscosity correctly in this strongly radiation pressure dominated flow for a wide range of optical depth.

The paper is organized as follows. We list the equations we solve in Section 2 and describe the simulation setup in Section 3. The main properties of the disks from the simulations are given in Section 4. Implications of the simulations are discussed in Section 5. Finally, the results are summarized in Section 6.

## 2. EQUATION

We solve the following set of ideal MHD equations coupled with the time dependent radiative transfer equations as

$$\begin{aligned} \frac{\partial \rho}{\partial t} + \nabla \cdot (\rho \mathbf{v}) &= 0, \\ \frac{\partial(\rho \mathbf{v})}{\partial t} + \nabla \cdot (\rho \mathbf{v} \mathbf{v} - \mathbf{B} \mathbf{B} + \mathbf{P}^*) &= -\mathbf{S}_r(\mathbf{P}) - \rho \nabla \phi, \\ \frac{\partial E}{\partial t} + \nabla \cdot [(E + P^*) \mathbf{v} - \mathbf{B}(\mathbf{B} \cdot \mathbf{v})] &= -c S_r(E) - \rho \mathbf{v} \cdot \nabla \phi, \\ \frac{\partial \mathbf{B}}{\partial t} - \nabla \times (\mathbf{v} \times \mathbf{B}) &= 0. \end{aligned} \quad (1)$$

$$\frac{\partial I}{\partial t} + \mathbf{c} \mathbf{n} \cdot \nabla I = S(I, \mathbf{n}). \quad (2)$$

Here,  $\rho$ ,  $\mathbf{B}$ ,  $\mathbf{v}$  are density, magnetic field and flow velocity,  $\mathbf{P}^* \equiv (P_g + B^2/2)\mathbf{I}$  (with  $\mathbf{I}$  the unit tensor),  $P_g$  is the gas pressure, and the magnetic permeability  $\mu = 1$ . The total gas energy density is

$$E = E_g + \frac{1}{2} \rho v^2 + \frac{B^2}{2}, \quad (3)$$

where  $E_g = P_g/(\gamma - 1)$  is the internal gas energy density with adiabatic index  $\gamma = 5/3$ . Gas temperature is calculated as  $T = P_g/R_{\text{ideal}}\rho$ , where  $R_{\text{ideal}}$  is the ideal gas constant with mean molecular weight  $\mu = 0.6$ .

These equations are similar as the ones we solve in Jiang et al. (2014a,b), except that we do not expand the radiation source terms  $\mathbf{S}_r(\mathbf{P})$ ,  $S_r(E)$  and  $S(I, \mathbf{n})$  to the first order of  $v/c$ . Instead, the lab frame specific intensity  $I(\mathbf{n})$  with angle  $\mathbf{n}$  is first transformed to the co-moving frame intensity  $I_0(\mathbf{n}_0)$  with angle  $\mathbf{n}_0$  via Lorentz transformation (e.g., Mihalas & Mihalas 1984). The source terms to describe the interactions between gas and radiation in the co-moving frame are

$$\begin{aligned} S(I_0, \mathbf{n}_0) = & c\rho\kappa_{aR} \left( \frac{a_r T^4}{4\pi} - I_0 \right) + c\rho\kappa_s (J_0 - I_0) \\ & + c\rho(\kappa_{aP} - \kappa_{aR}) \left( \frac{a_r T^4}{4\pi} - J_0 \right) \\ & + c\rho\kappa_s \frac{4(T - T_r)}{T_e} J_0. \end{aligned} \quad (4)$$

Here  $\kappa_{aR}$  and  $\kappa_{aP}$  are the Rosseland and Planck mean absorption opacities while  $\kappa_s$  is the electron scattering opacity. The angular quadrature of the specific intensity in the co-moving frame is  $J_0 = \int I_0(\mathbf{n}_0) d\Omega_0$ . The last term in the above equation is an approximate way to mimic the energy exchange via Compton scattering (Hirose et al. 2009; Jiang et al. 2013a, 2014a), where  $T_r \equiv (4\pi J_0/a_r)^{1/4}$  with the radiation constant  $a_r = 7.57 \times 10^{15} \text{ erg cm}^{-3} \text{ K}^{-4}$  is the radiation temperature and  $T_e = 5.94 \times 10^9 \text{ K}$  is the effective temperature for electron rest mass. All the source terms are added implicitly as in Jiang et al. (2014b). After the specific intensities  $I_0(\mathbf{n}_0)$  are updated in the co-moving frame, they are transformed back to the lab frame via Lorentz transformation. Then the radiation momentum and energy source terms  $\mathbf{S}_r(\mathbf{P})$  and  $S_r(E)$  are calculated by the differences between the angular quadratures of  $I(\mathbf{n})$  in the lab frame before and after adding the source terms. It can be easily confirmed that for the absorption source terms in equation 4, only the Planck mean absorption opacity  $\kappa_{aP}$  enters the energy equation while the momentum source term only contains the Rosseland mean opacity  $\kappa_{aR}$ , which are consistent with the radiation moment equations we solve in Jiang et al. (2012) and Jiang et al. (2013a) to the first order  $v/c$ . The source term for Compton scattering also only affects the radiation energy density but not momentum in the co-moving frame. The transport step in equation (2) is solved in the same way as in Jiang et al. (2014b). We are able to reproduce all the test problems described in Jiang et al. (2014b) and the new algorithm has been successfully used to study stream-stream collisions in tidal disruption events (Jiang et al. 2016c).

Following Jiang et al. (2016b), in order to capture the important effects caused by the iron opacity bump in AGN accretion disks, we calculate the total Rosseland mean opacity based on the same opacity table as in Figure 2 of Jiang et al. (2015). We then subtract the electron scattering value  $\kappa_{\text{es}} = 0.34 \text{ cm}^2 \text{ g}^{-1}$  to get the Rosseland mean absorption opacity  $\kappa_{aR}$ . As we do not have any Planck mean opacity table, we only include the Planck mean free-free absorption opacity

$\kappa_{aP} = 3.7 \times 10^{53} (\rho^9/E_g^7)^{1/2} \text{ cm}^2 \text{ g}^{-1}$ , which is the most important absorption opacity of the disk in the super-Eddington regime.

A pseudo-Newtonian potential (Paczynsky & Wiita 1980) is used to mimic the general relativity effects around a Schwarzschild black hole as

$$\phi = -\frac{GM_{\text{BH}}}{r - 2r_g}, \quad (5)$$

where  $G$  is the gravitational constant,  $M_{\text{BH}}$  is the black hole mass,  $r$  is the distance to the central black hole and  $r_g \equiv GM_{\text{BH}}/c^2$  is the gravitational radius. Notice that the innermost stable circular orbit of this potential is  $r_{\text{ISCO}} = 6r_g$ .

We solve the above equations with the new radiation MHD code *Athena++* (Stone et al. 2008, Stone et al. 2017, in preparation) in the spherical polar coordinate system  $(r, \theta, \phi)$ . Logarithmic grid is used for the radial direction so that we can cover a large dynamic range. Static mesh refinement is used to increase the resolution near the disk midplane but not the polar regions, which significantly reduces the computational cost compared with the case without any refinement for the same effective resolution. We refine  $r, \theta, \phi$  directions simultaneously to achieve the same resolution for all three directions at each level. The fiducial parameters for all the simulations are summarized in Table 1 and details of the simulation setup are described below.

### 3. SIMULATION SETUP

We carry out four simulations AGN150, AGN33, AGNB25 and AGNB52 to explore the properties of super-Eddington accretion disks around a  $5 \times 10^8 M_\odot$  black hole with different accretion rates and magnetic field topologies. All the simulations cover a radial range from the inner boundary  $4r_g$  to the outer boundary  $1600r_g$  with 64 grids, 0 to  $\pi$  along the  $\theta$  direction with 32 grids and 0 to  $2\pi$  along  $\phi$  direction with 64 grids in the coarse level. With logarithmic grid along the radial direction, we can keep  $\Delta r/r = \Delta\theta = \Delta\phi$ . We refine the region within  $20^\circ$  along  $\theta$  direction on both sides of the disk midplane and radii smaller than  $80r_g$  with 2 or 3 levels of refinement (see Table 2). Periodic boundary conditions are used for  $\phi$  boundary. For the polar boundary condition, the variables in the ghost zones are copied from the last active zones at the same  $r$  but with  $\phi$  differing by  $180^\circ$ . The same mapping is also done for specific intensities propagating along the same direction. Vacuum boundary conditions are used for the specific intensities in the inner and outer radial boundaries, which means in the ghost zones, outgoing specific intensities are copied from the last active zones, while incoming specific intensities are set to be zero. All the gas and magnetic field quantities are copied from the last active zones to the ghost zones except  $v_r$ , which is only copied if  $v_r$  in the last active zones points outward. In other cases,  $v_r$  is set to be zero in the ghost zones.

Initially, we set up a hydrostatic equilibrium rotating torus (Hawley 2001; Kato et al. 2004) centered at  $r_i = 80r_g$ , except the run AGNB25, where the center of the torus is at  $r_i = 50r_g$  as in Jiang et al. (2014a). The radial profile of the specific angular momentum of the torus  $l$  is assumed to be  $l = l_i (r \sin \theta / r_i)^{0.4}$ , where  $l_i$  is

**Table 1**  
Fiducial Simulation Parameters

Parameters	Values	Definition
$M_{\text{BH}}$	$5.00 \times 10^8 M_{\odot}$	Black Hole Mass
$r_g \equiv GM_{\text{BH}}/c^2$	$7.42 \times 10^{13} \text{ cm}$	Gravitational Radius
$\kappa_{\text{es}}$	$0.34 \text{ g cm}^{-2}$	Electron Scattering Opacity
$L_{\text{Edd}} \equiv 4\pi GM_{\text{BH}}c/\kappa_{\text{es}}$	$7.39 \times 10^{46} \text{ erg s}^{-1}$	Eddington Luminosity
$\dot{M}_{\text{Edd}} \equiv 10L_{\text{Edd}}/c^2$	$8.22 \times 10^{26} \text{ g s}^{-1}$	Eddington Accretion Rate
$\rho_0$	$1.00 \times 10^{-8} \text{ g cm}^{-3}$	Fiducial Density
$T_0$	$2.00 \times 10^5 \text{ K}$	Fiducial Temperature
$P_0$	$2.77 \times 10^5 \text{ dyn cm}^{-2}$	Fiducial Pressure
$v_0$	$5.26 \times 10^6 \text{ cm s}^{-1}$	Fiducial Velocity
$t_0 \equiv r_g/c$	$2.48 \times 10^3 \text{ s}$	Fiducial Time
$B_0$	$1.87 \times 10^3 \text{ G}$	Fiducial Magnetic Field

**Table 2**  
Simulation Parameters

Variables/Units	AGN150	AGN33	AGNB25	AGNB52
$r_i/r_g$	80	80	80	50
$\rho_i/\rho_0$	50	10	10	10
$T_i/T_0$	12.4	8.4	8.3	8.4
$\langle P_r/P_g \rangle$	$7.53 \times 10^2$	$3.02 \times 10^3$	$2.86 \times 10^3$	$1.81 \times 10^4$
$\langle P_r/P_g \rangle_{\rho}$	$4.94 \times 10^2$	$7.81 \times 10^2$	$7.40 \times 10^2$	$7.98 \times 10^2$
$\langle P_B/P_g \rangle$	21.55	47.27	3.25	0.11
$\langle P_B/P_g \rangle_{\rho}$	$6.77 \times 10^{-4}$	$8.83 \times 10^{-3}$	$8.52 \times 10^{-3}$	$4.65 \times 10^{-2}$
$\Delta r/r$	0.024	0.012	0.012	0.012
$\Delta \theta$	0.024	0.012	0.012	0.012
$\Delta \phi$	0.024	0.012	0.012	0.012
$N_n$	80	80	80	80
$B$ Loops	Multiple	Multiple	Single	Single

Note: The center of the initial torus is located at  $r_i$  with density and temperature to be  $\rho_i$  and  $T_i$ . For any quantity  $a$ ,  $\langle a \rangle$  is the volume averaged value over the torus while  $\langle a \rangle_{\rho}$  is the averaged value weighted by the mass in each cell. The grid sizes  $\Delta r, \Delta \theta, \Delta \phi$  are for the finest level at the center of the torus. The number of angles for the radiation grid is  $N_n$  in each cell.

the Keplerian value of the specific angular momentum at  $r_i$ . With this torus shape, the inner edges of the torus are at  $40r_g$  and  $30r_g$  with  $r_i = 80r_g$  and  $50r_g$  respectively. In this way, we do not put any mass inside the region where a steady state disk is going to be formed. The density maximum at the center of the torus  $\rho_i$  is a free parameter, which determines the accretion rate we will get. The larger  $\rho_i$  is, the larger the accretion rate we can achieve. We also assign a total pressure  $\rho_i v_i^2 (\rho/\rho_i)^\gamma / \gamma$  with  $v_i$  as a free parameters, which is then replaced by the sum of gas and radiation pressure by assuming thermal equilibrium. The density and temperature at the center of the torus, along with the averaged ratios between radiation and gas pressure for the four runs are summarized in Table 2. Specific intensities are initialized isotropically in the torus as in Jiang et al. (2014a), which adjust within a few steps to give the correct flux. Random perturbations with 1% amplitude are added to the density to seed the MRI turbulence. Outside the torus, all the variables are set to the floor values with density floor  $10^{-8}\rho_0$ , temperature floor  $10^{-2}T_0$  and specific intensity floor  $10^{-8}a_r T_0^4$ .

Two different initial magnetic field topologies are used in the four simulations. For runs AGNB25 and AGNB52, we assume  $\phi$  component of the vector potential is proportional to the density while other components are zero. Magnetic fields are then initialized with the vector potential, which have the shape of a single loop in the torus. When the inner part of the torus is accreted towards the black hole in this case, all the magnetic fields will have the same sign of  $B_\theta$  and net magnetic flux through the disk is expected. For runs AGN150 and AGN33, the vector potential is constructed in the similar way as in the Appendix A of Penna et al. (2013) to create multiple loops of magnetic fields in the torus. We construct two loops with the inner edge of the magnetized region at  $r_i - 20r_g$  while the outer edge at  $r_i + 40r_g$ . There are two differences compared with Penna et al. (2013). First, we scale the vector potential to the density instead of internal energy. Second, we multiply the vector potential by the factor  $\sin(\pi/2 - \theta)$  so that the magnetic field loops change sign across the disk midplane. Properties of the initial torus and the resolutions for the four runs are summarized in Table 2.

These simulations are costly, and were run on 512 – 4096 nodes of the Mira supercomputer at ALCF for a total of 35M core hours. Access to this system was provided by the DOE INCITE program, which has been essential for this work.

#### 4. RESULTS

MRI develops in the initial torus and drives the gas flowing towards the central black hole. An accretion disk is built up self-consistently inside the inner edge of the torus. We do not control the mass accretion rate in this setup. Instead, it is determined by the available mass in the torus and mechanisms for angular momentum transfer as calculated by the code. The region where a steady state accretion disk is formed will be the focus of our analysis.

##### 4.1. Simulation History

The net mass accretion rate through each radius  $r$  can be calculated as

$$\dot{M} = \int_0^{2\pi} \int_0^\pi \rho v_r r^2 \sin \theta d\theta d\phi. \quad (6)$$

Histories of  $\dot{M}$  at  $10r_g$  for the four simulations are shown in Figure 1. After the initial  $\sim 10^4 t_0$ , the disks have extended to  $10r_g$  with time averaged  $\dot{M}$  reaching  $-146.2, -33.2, -25.8, -51.9 \dot{M}_{\text{Edd}}$  for the four runs AGN150, AGN33, AGNB25, AGNB52 respectively. The mass accretion rates show significant fluctuations due to turbulence.

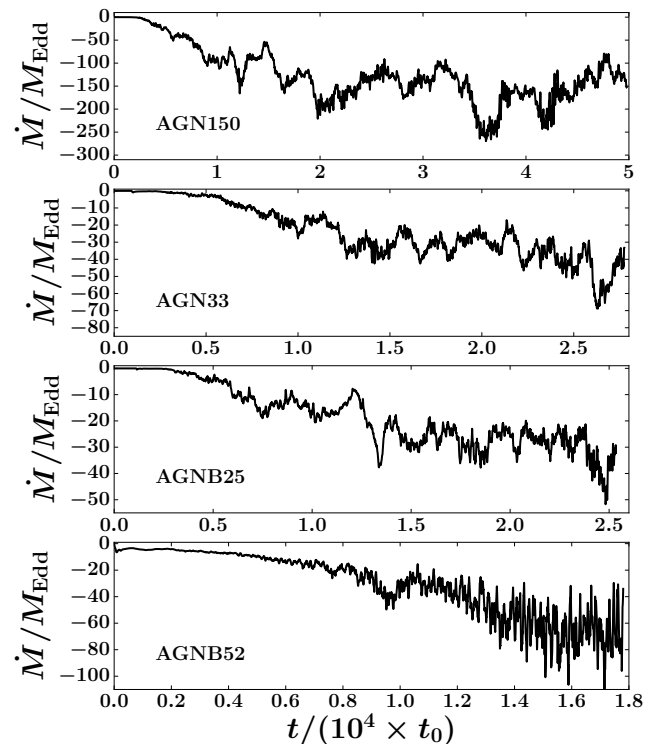


**Figure 1.** Histories of spherically integrated mass accretion rate at  $10r_g$  for the four simulations. Negative values of  $\dot{M}$  mean gas flows towards the black hole. The time unit  $t_0 \equiv r_g/c$  corresponds to  $5 \times 10^{-3}$  Keplerian orbital period at  $10r_g$ .

All the four runs reach accretion rates significant above  $\dot{M}_{\text{Edd}}$  despite different initial magnetic field topologies, although the disks have quite different structures. Histories of the azimuthally averaged  $\theta$  profiles of density  $\rho$ , radiation temperature  $T_r$  and azimuthal component of magnetic field  $B_\phi$  at  $20r_g$  are shown in Figure 2 for the two runs AGN33 and AGNB52. The space-time diagrams for runs AGN150 and AGNB25 are similar to the left and right panels of Figure 2 respectively. The main differences of the two runs are the evolution of  $B_\phi$ . In the run AGNB52, after the disk is formed at  $20r_g$ ,  $B_\phi$  reverses starting near the disk midplane roughly every  $4000t_0$ , which corresponds to  $\sim 7$  Keplerian rotation periods at this location. The magnetic fields also rise up from the disk midplane due to buoyancy. This is the well known butterfly diagram, which has been observed in previous

global simulations with (Jiang et al. 2014a) or without (O’Neill et al. 2011) radiative transfer, as well as various local shearing box simulations of MRI turbulence (Stone et al. 1996; Miller & Stone 2000; Shi et al. 2010; Davis et al. 2010; Simon et al. 2012; Jiang et al. 2013a, 2014b), although the periods for field reversal can differ slightly in these simulations. The butterfly diagram is believed to be generated by the dynamo process of MRI (Brandenburg et al. 1995; Blackman 2012) and it is an indication that magnetic pressure is amplified so that magnetic buoyancy can play a significant role. However, a similar butterfly diagram is not observed in the run AGN33. Although  $B_\phi$  shows small scale turbulent structures and undergoes vertical oscillations in AGN33, we do not see any field reversal and systematic buoyantly rising magnetic field from the disk midplane. This suggests that MRI turbulence is much weaker in this case and other mechanisms must be responsible for the angular momentum transfer so that the simulations AGN150 and AGN33 can reach similar accretion rates as in AGNB25 and AGNB52. This will be examined in Section 4.5.

The vertical profiles of density are more concentrated towards the disk midplane in AGNB52 compared with the density profiles in AGN33 as shown in Figure 2. Particularly, it happens when strong magnetic fields buoyantly rise up from the disk midplane. This is consistent with the simulation shown in Jiang et al. (2014a) and is closely related to the butterfly diagram. The strong magnetic buoyancy in AGNB52 moves the dissipation away from the disk midplane and reduces the disk scale height compared with the case without strong magnetic buoyancy as in AGN33. The radiation temperature varies from  $\sim 10^5 - 10^6$  K and the midplane temperature is larger in AGNB52 because of the larger accretion rate.

#### 4.2. Spatial Structures of the Disks

Snapshots of density  $\rho$  and radiation energy density  $E_r$  at the inner regions of the accretion disks for AGN33 and AGNB25 are shown in Figure 3. In both cases, the density structures are fully turbulent as in previous 3D global accretion disk simulations with MRI turbulence (Armitage 1998; Hawley 2001; Jiang et al. 2014a). The striking features are the spiral arms in the snapshots of radiation energy density, which also show up in the snapshots of density in spite of the turbulence. The spiral structures exist in all the four runs and they cause significant azimuthal variations of density and temperature. Excitations of density waves and the associated spiral shocks by the MRI turbulence have been observed in previous local (Gardiner & Stone 2005) and global (Armitage 1998) simulations and have been suggested to be caused by the generic swing application process driven by the potential vorticity (Heinemann & Papaloizou 2009a,b). This is the first time that the development of coherent global density waves and spiral shocks have been seen in simulations with self-consistent thermodynamics in the strongly radiation pressure dominated AGN accretion disks. Unlike the weak spiral shocks and small associated Reynolds stress found in previous calculations, we will show in Section 4.5 that the density waves generate very strong shocks in our simulations and result in very large Reynolds stress.

Slices of  $E_r$  as well as radial and poloidal components of radiation flux  $F_{r,r}$ ,  $F_{r,\theta}$  through the plane  $\phi = \pi$  at the

same times are shown in Figure 4. Locations of sharp  $E_r$  jumps are caused by the spiral shocks, which extend to large angles along the  $\theta$  direction. Multiple shock positions correspond to the spiral arms shown in Figure 3. The lab frame radiation flux is dominated by the advection component  $vE_r$  in the main body of the disk. Then photons leave the disk through the low density funnels.

Time averaged spatial structures of the disks are studied during the periods  $2.05 \times 10^4 - 4.98 \times 10^4 t_0$ ,  $1.71 \times 10^4 - 2.78 \times 10^4 t_0$ ,  $1.71 \times 10^4 - 2.54 \times 10^4 t_0$ ,  $1.37 \times 10^4 - 1.78 \times 10^4 t_0$  for runs AGN150, AGN33, AGNB25 and AGNB52 respectively, which are chosen when the inner regions of the disks have reached an approximately constant  $\dot{M}$  (see Section 4.3). This is also the time range we will average the data for the following analysis. We calculate the time and azimuthally averaged  $\rho$ ,  $\rho v_r$ ,  $\rho v_\theta$ ,  $E_r$ ,  $B_r$ ,  $B_\theta$ , where  $v_r$ ,  $B_r$  and  $v_\theta$ ,  $B_\theta$  are the radial and poloidal components of the flow velocity and magnetic fields. The averaged momentum is then divided by the averaged density to get the density weighted flow velocity. These averaged quantities at the inner region of the disks for the four runs are shown in Figure 5 and 6. The spiral shock structures do not show up after the azimuthal average. Gas flows towards the black hole near the disk midplane while strong outflow with velocity  $\sim 0.1 - 0.4c$  develops along the low density funnels. Despite the different magnetic field configurations, the runs AGN33 and AGNB25 show very similar time averaged structures when they reach similar accretion rates. Magnetic pressure in the funnel region is much stronger in runs AGNB25 and AGNB52 when there are net poloidal magnetic field lines through the disks. The stagnation points in the funnels, where the velocities change from inflow to outflow, are located at  $\sim 10 - 20 r_g$ , except for the run AGN150. When  $\dot{M}$  reaches  $\sim 200 \dot{M}_{\text{Edd}}$ , the stagnation points move to  $\sim 50 - 60 r_g$  and all the funnel becomes optically thick in this region. As outflow is now launched from a much larger radius, the outflow velocity is actually smaller in this case. Properties of the outflow will be quantified in Section 4.6.

#### 4.3. Radial Profiles of the Disks

For any quantity  $a$ , we calculate the time and shell averaged value at each radius  $r$  as

$$\langle\langle a \rangle\rangle = \frac{1}{4\pi\Delta t} \int_0^{2\pi} \int_0^\pi \int_{t_1}^{t_2} a \, dt \sin\theta d\theta d\phi, \quad (7)$$

where  $\Delta t = t_2 - t_1$  with the time interval  $t_1, t_2$  as specified in Section 4.2. The mass weighted average is calculated as

$$\langle\langle a \rangle\rangle_\rho = \frac{1}{4\pi\Delta t \langle\langle \rho \rangle\rangle} \int_0^{2\pi} \int_0^\pi \int_{t_1}^{t_2} a \rho \, dt \sin\theta d\theta d\phi. \quad (8)$$

Radial profiles of the average net mass accretion rates  $\langle\langle \dot{M} \rangle\rangle$  (equation 6) for the four runs AGN150, AGN33, AGNB25, AGNB52 are shown in Figure 7. The net mass accretion rates roughly reach constant values up to  $35 r_g$  for AGN150, AGN33,  $25 r_g$  for AGNB25 and  $20 r_g$  for AGNB52 during the time we have run these simulations, which indicate steady state disks in these regions. The net mass accretion rates can be decomposed into two components with  $v_r > 0$  and  $v_r < 0$ , which are also

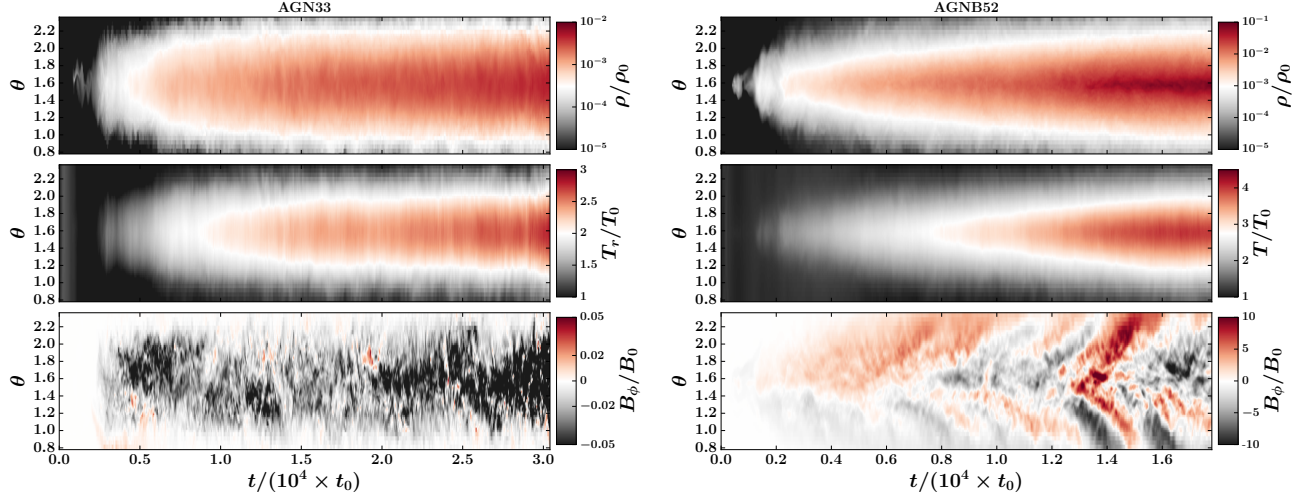


**Figure 2.** Space-time diagram of azimuthally averaged density (top panels), radiation temperature (middle panels) and azimuthal component of magnetic field (bottom panels) at radius  $20r_g$  for the run AGN33 (left) and AGNB52 (right). (Note that the color bar ranges differ between the left and right panels.) The butterfly diagram shows up in the run AGNB52 where a single loop of magnetic field is used initially but does not exist in AGN33 which adopts multiple loops of magnetic field in the initial torus.

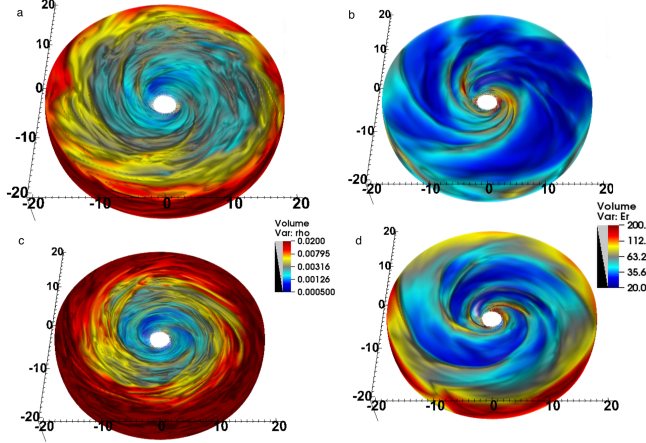


**Figure 3.** Snapshots of density  $\rho/\rho_0$  (left panels a and c) and radiation energy density  $E_r/a_r T_0^4$  (right panels b and d) at the inner  $40r_g$  of the accretion disks for runs AGN33 (top panels a and b) and AGNB25 (bottom panels c and d). The length unit in the plot is  $2r_g$ . The snapshots are taken at times  $2.73 \times 10^4 t_0$  and  $2.53 \times 10^4 t_0$  for runs AGN33 and AGNB25 respectively. Notice the significant spiral arms in the disk, particularly for  $E_r$ .

shown in Figure 7 for comparison with the net accretion rate. The mass fluxes associated with the ingoing and outgoing components are much larger than  $\dot{M}$ , but this is predominantly due to turbulent motions in the flow. In particular, the outgoing component always begins outside ISCO, as expected, and increase rapidly with radius. We emphasize that only a small fraction of this outgoing component is associated with an unbound outflow, which will be quantified in Section 4.6. It is interesting to notice that these inflow and outgoing components are much larger than the stellar mass black hole case for a similar net mass accretion rate  $\dot{M}/\dot{M}_{\text{Edd}}$  (Figure 4 of Jiang et al. 2014a).

The surface density  $\Sigma$  at each radius can be calculated as  $\Sigma = \int_0^{2\pi} \int_0^\pi \rho r \sin \theta d\theta d\phi$ . The time averaged radial profiles of  $\Sigma$  multiplied by the electron scattering opacity  $\kappa_{\text{es}}$  are shown in the top panels of Figure 8 for the

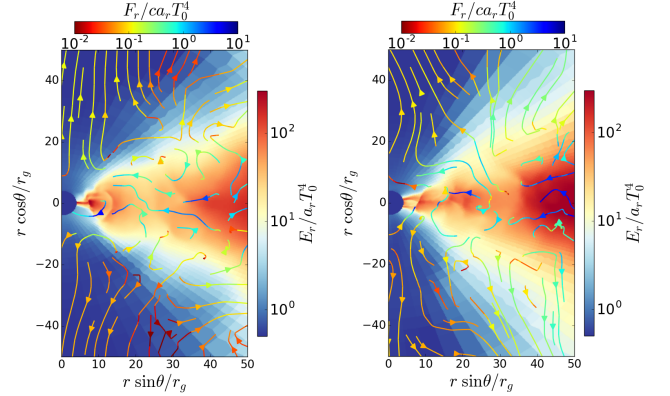


**Figure 4.** Slices of radiation energy density  $E_r$  (color) and  $r, \theta$  components of radiation flux  $F_{r,r}$ ,  $F_{r,\theta}$  (streamlines) through the plane  $\phi = \pi$  at the same times as in Figure 3 for the two runs AGN33 (left panel) and AGNB25 (right panel).

four simulations. The total optical depth is always larger than  $10^3$  and the largest in AGN150, corresponding to the largest accretion rate. In each simulation, surface density increases with radius as  $r^{1.8}$  for AGN150, AGN33,  $r^{2.0}$  for AGNB25 and  $r^{2.8}$  for AGNB52, which is consistent with the density profiles shown in Jiang et al. (2014a). Similar to the stellar mass black hole case, the effective absorption opacity in the inner regions of these disks is much smaller and approaches optically thin regime. Gas and radiation temperature can differ slightly even near the disk midplane as shown in Section 4.4.

The time and shell averaged radial profiles of isotropic radiation pressure ( $P_r = E_r/3$ ), gas pressure  $P_g$  and magnetic pressure  $P_B$  are shown in the second panels of Figure 8. The ratio between radiation and gas pressure varies from  $10^3$  to  $10^5$ , which is significantly larger than the ratio in the stellar mass black hole case as shown in Figure 9 of Jiang et al. (2014a). For runs AGN150 and AGN33 where there are no net vertical magnetic flux through the disk, radiation pressure is larger than the magnetic pressure by a factor of  $10^4$ – $10^5$ . However, with net vertical magnetic fields threading the disk as in runs AGNB25 and AGNB52, the ratio between radiation and



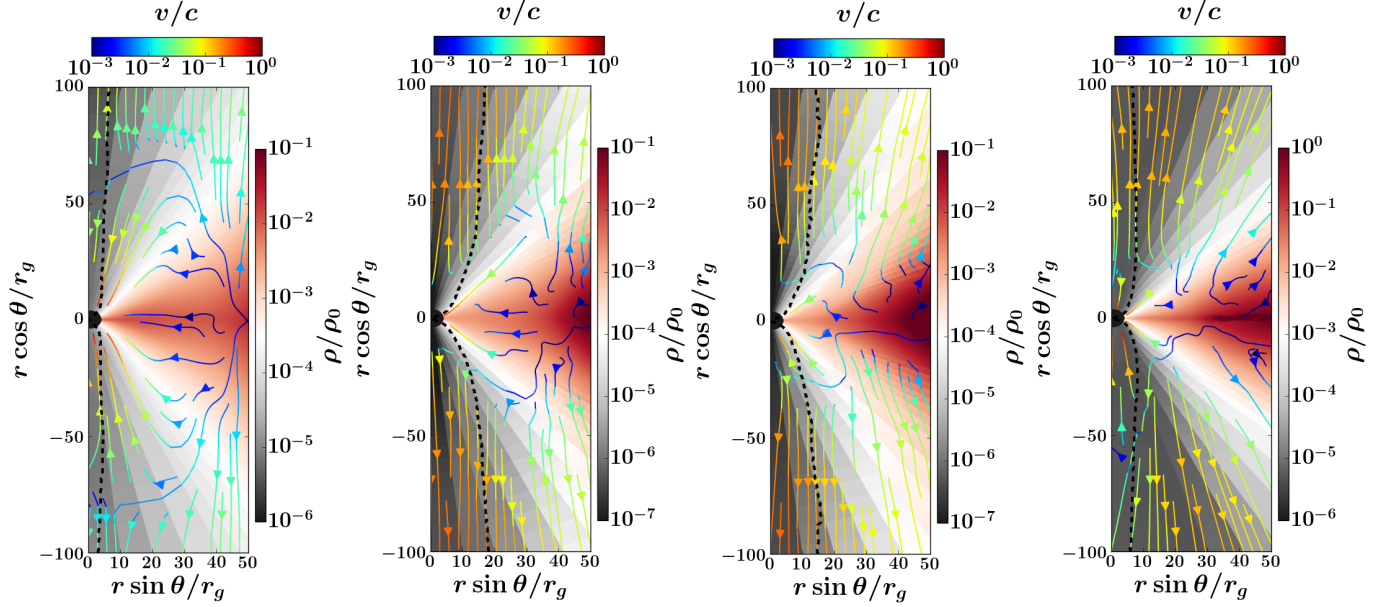


**Figure 5.** Time and azimuthally averaged spatial structures of density  $\rho$  (color) and density weighted flow velocity  $v_r, v_\theta$  (streamlines) at the inner regions of the disks. Color of the streamlines represents the velocity magnitude  $v \equiv \sqrt{v_r^2 + v_\theta^2}$ . From left to right, they are for runs AGN150, AGN33, AGNB25, AGNB52 respectively. The dashed black lines indicate the locations where the integrated optical depth from the rotation axis along the horizontal direction is one.

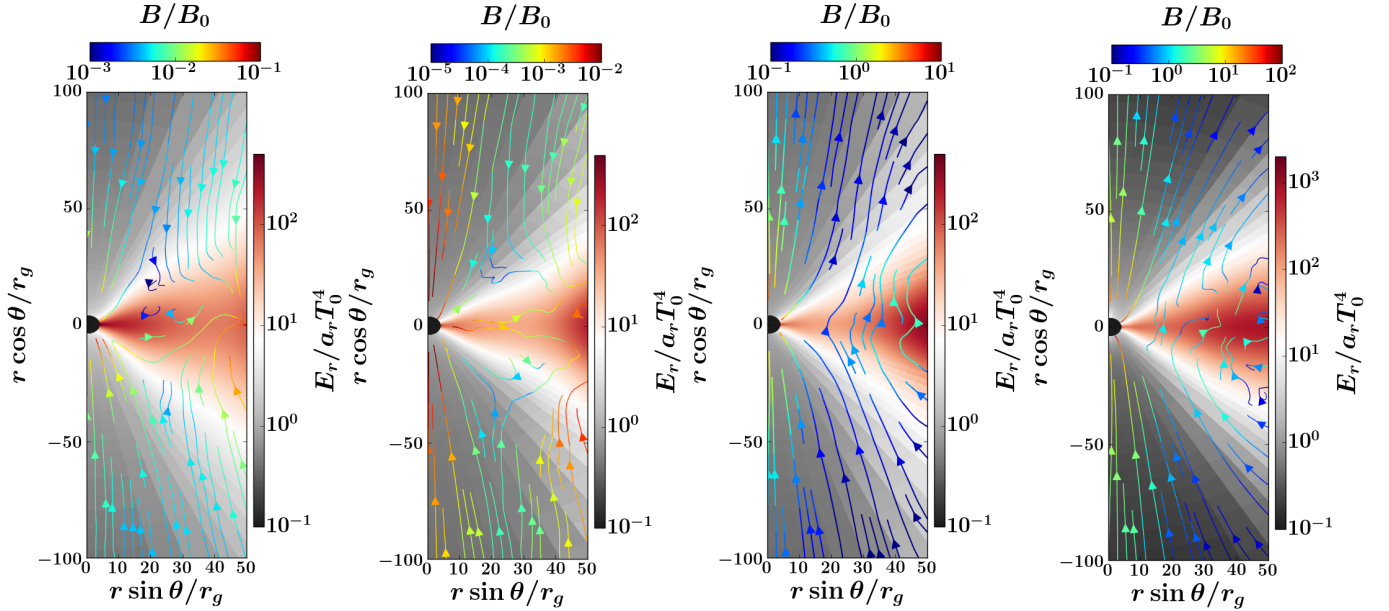


**Figure 6.** Time and azimuthally averaged spatial structures of radiation energy density  $E_r$  (color) and magnetic fields  $B_r, B_\theta$  (streamlines). Color of the streamlines represent  $B \equiv \sqrt{B_r^2 + B_\theta^2}$ . From left to right, they are for runs AGN150, AGN33, AGNB25, AGNB52 as in Figure 5. The time average is also done during the same time as in that Figure. There are net vertical magnetic fields through the disk in the third and fourth panels but not in the first two panels.

magnetic pressure varies from 5 to 50, which is consistent with the values found in previous local shearing box and global simulations of MRI turbulence in radiation pressure dominated flows when the radiation pressure is only a factor of a few larger than the gas pressure (Hirose et al. 2009; Jiang et al. 2013a, 2014a).

Stress responsible for the angular momentum transfer in the disk comes from Maxwell stress  $S_m$ , Reynolds stress  $S_h$  and radiation stress  $S_{rad}$ . In spherical polar

coordinate, we calculate the radial profiles of the volume and time averaged  $r - \phi$  stress as  $S_m = \langle \langle -B_r B_\phi \rangle \rangle$ ,  $S_h = \langle \langle \rho v_r v_\phi \rangle \rangle - \langle \langle \rho v_r \rangle \rangle \langle \langle v_\phi \rangle \rangle$ . Here for the Reynolds stress, we subtract the angular momentum flux carried by the mean inflow in the disk. Similarly, the off-diagonal component of radiation pressure in the lab-frame  $P_r^{\phi}$  includes contributions from radiation viscosity in the co-moving frame as well as the inflow angular momentum flux carried by the radiation when photons are



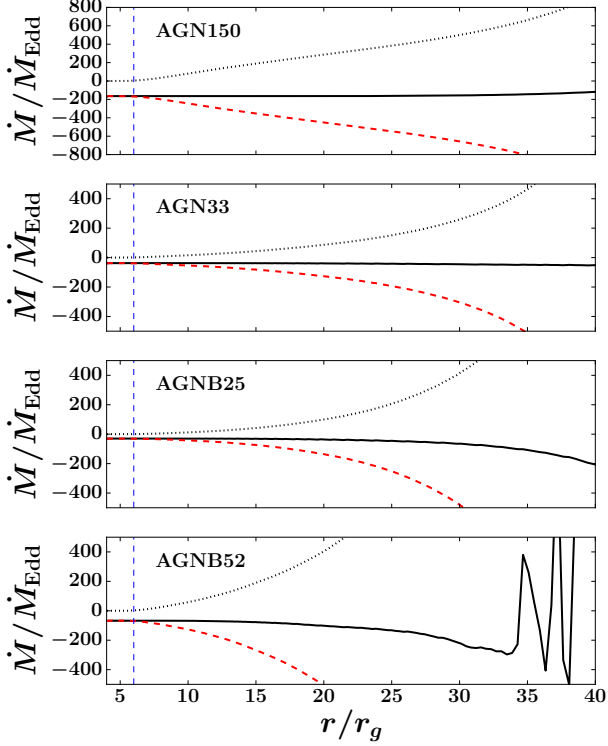


**Figure 7.** Time and shell averaged radial profiles of mass accretion rate  $\dot{M}$  in unit of the Eddington mass accretion rate  $\dot{M}_{\text{Edd}}$  defined in Table 1. From top to bottom, they are for the four runs AGN150, AGN33, AGNB25, AGNB52. In each panel, the solid black lines are the net mass accretion rates  $\dot{M}$ , which are  $-150, -33, -25, -52\dot{M}_{\text{Edd}}$  in the steady state inner regions of the disks. The dotted black and dashed red lines are the mass flux carried by the gas with  $v_r > 0$  and  $v_r < 0$  respectively. The dashed vertical lines indicate the location of ISCO ( $6r_g$ ).

advected inwards with the mean accretion flow. This contribution is included by the Lorentz transformation of the specific intensities due to the azimuthally averaged radial inflow  $\langle v_r \rangle$  and rotation velocities  $\langle v_\phi \rangle$  (see discussions in Section 5.2). To subtract this component, we transform specific intensity  $E_{r,0}/4\pi$  for each angle from the co-moving frame to the lab-frame with velocity  $\langle v_r \rangle$  and  $\langle v_\phi \rangle$ , where  $E_{r,0}$  is the radiation energy density in the co-moving frame. The off-diagonal component of the second moment of these new lab-frame intensities is then subtracted from  $P_r^{r\phi}$ , the result of which is  $S_{rad}$ . The corresponding effective  $\alpha$  values can be defined as  $\alpha_m \equiv S_m/(\langle\langle P_r \rangle\rangle + \langle\langle P_g \rangle\rangle + \langle\langle P_B \rangle\rangle)$ ,  $\alpha_h \equiv S_h/(\langle\langle P_r \rangle\rangle + \langle\langle P_g \rangle\rangle + \langle\langle P_B \rangle\rangle)$ ,  $\alpha_r \equiv S_{rad}/(\langle\langle P_r \rangle\rangle + \langle\langle P_g \rangle\rangle + \langle\langle P_B \rangle\rangle)$ . Radial profiles of the averaged stresses and effective  $\alpha$  values for the four runs are shown in Figure 8. For the two runs with multiple magnetic field loops (AGN150 and AGN33), Reynolds stress is actually larger than the Maxwell stress by a factor of  $10^3$ . The Maxwell stress increases significantly when a single loop of magnetic fields is used as in AGNB25 and it only becomes larger than the Reynolds stress in the run AGNB52 when the net poloidal magnetic flux through the disk is increased by a factor of  $\sim 2 - 4$  in the inner region of the disk. The relative small Maxwell stress in AGN150 and AGN33 is also consistent with the small magnetic pressure in the

two runs, as the ratio between  $\langle\langle -B_r B_\phi \rangle\rangle$  and  $\langle\langle P_B \rangle\rangle$  is always  $\sim 0.2 - 0.4$  in these simulations as found in most simulations with MRI turbulence (Blackman et al. 2008; Guan et al. 2009; Sorathia et al. 2012; Jiang et al. 2013b; Hawley et al. 2011, 2013; Jiang et al. 2014a). We have also checked that in all the four runs, the total magnetic pressure is dominated by the turbulent magnetic pressure with contributions from the mean magnetic fields component less than 10%. The time and volume averaged radial component of magnetic fields  $B_r$  is almost zero in all the four runs, which confirms that the Maxwell stress we get from these simulations are indeed due to the turbulence instead of the stress caused by the mean magnetic field components  $\langle B_r \rangle$  and  $\langle B_\phi \rangle$ .

The increased saturation level of Maxwell stress with net vertical magnetic flux through the disk has been found in various local shearing box as well as global simulations of MRI turbulence (Hawley et al. 1995; Bai & Stone 2013; Fromang et al. 2013; Simon et al. 2013; Béthune et al. 2016; Zhu & Stone 2017). However, in most of these ideal MHD simulations with isothermal equation of state, Maxwell stress is always larger than the Reynolds stress by a factor of 4–5. The ratio between Maxwell stress and total pressure is also larger than  $\sim 1 - 3\%$  in both cases with or without net vertical magnetic flux. For simulations of MRI turbulence in the radiation pressure dominated flows when the radiation pressure is only larger than the gas pressure by a factor of  $\sim 10$  and radiation sound speed is still much smaller than the speed of light (Hirose et al. 2009; Blaes et al. 2011; Jiang et al. 2013a, 2014a), similar results are found for the properties of MRI turbulence. However, Jiang et al. (2013b) studied the saturation of MRI turbulence in strongly radiation pressure dominated regime based on unstratified local shearing box simulations and found that when radiation pressure was more than 100 times larger than the gas pressure, the ratio between Maxwell stress and total pressure became smaller than 1%. This is likely caused by the damping due to radiation viscosity in the very compressible radiation pressure dominated flow and consistent with the results shown in Figure 8. In these local shearing box simulations, Reynolds stress is always smaller than the Maxwell stress and the ratio between Maxwell stress and Reynolds stress becomes larger in the strongly radiation pressure dominated regime. This is different from what we find in the four simulations. As we will show in Section 4.5, the large Reynolds stress in these global simulations is produced by the density waves as shown in Figure 3, which are much weaker in local shearing box simulations.

The sum of  $\alpha_h, \alpha_m$  and  $\alpha_r$  are almost the same as  $\alpha_h + \alpha_m$  as shown at the bottom panels of Figure 8 for all the four runs, which means radiation stress is much smaller than Maxwell and Reynolds stresses, even though the radiation pressure is much larger than the gas pressure. This is because the anisotropic component of the co-moving radial field is significantly reduced by the small mean free path to electron scattering. Even the relative contributions from Maxwell and Reynolds stresses vary significantly among the four runs, the ratio between the total stress and pressure is actually very similar. The effective  $\alpha$  varies from  $\sim 0.02$  at the outer edge of the steady state disk to  $\sim 0.1$  at the inner edge of

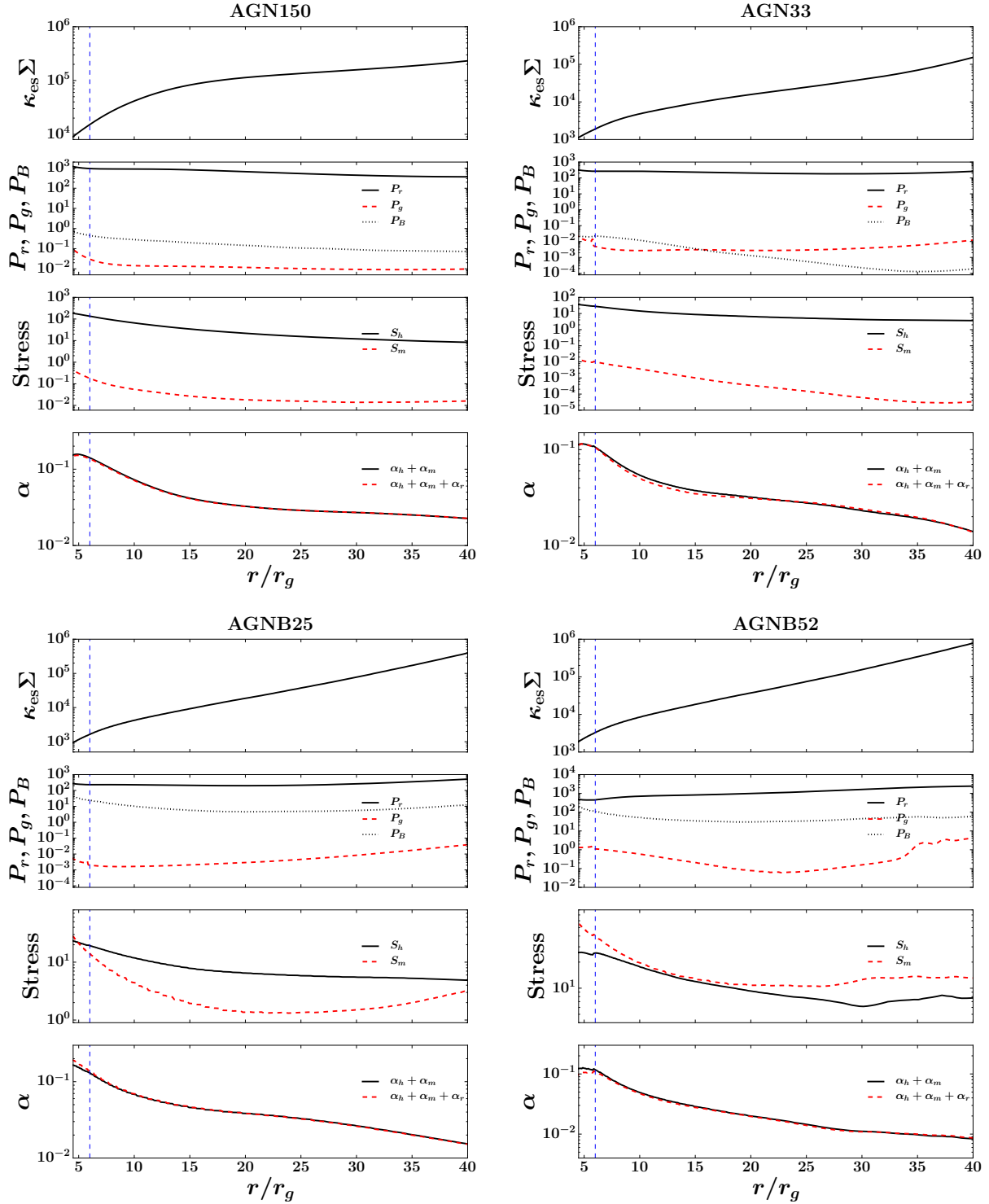


**Figure 8.** Time and shell averaged radial profiles of various quantities as described in Section 4.3 for the four runs as indicated in the figures. From top to bottom panels of each plot, they are surface density multiplied by the electron scattering opacity  $\kappa_{\text{es}}$ , radiation ( $P_r$ , black solid lines), gas ( $P_g$ , red dashed lines) and magnetic ( $P_m$ , black dotted lines) pressure, Reynolds ( $S_h$ , black solid lines) and Maxwell ( $S_m$ , red dashed lines) stress, effective  $\alpha$  for Reynolds and Maxwell stress alone ( $\alpha_h + \alpha_m$ , black solid lines) as well as effective  $\alpha$  including the radiation viscosity ( $\alpha_h + \alpha_m + \alpha_r$ , red dashed lines). The vertical dashed lines show the location of ISCO. Pressure and stress have the fiducial units given in Table 1.

the simulation domain for all the four runs as shown in the bottom panels of Figure 8, which is also similar to the profile we get for the stellar mass black hole case (Jiang et al. 2014a). This is perhaps why all these disks can reach such high accretion rates despite different mechanisms controlling the transfer of angular momentum.

#### 4.4. Vertical Structures of the Disks

We use the disks at  $20r_g$  from simulations AGN33 and AGNB52 as examples to study the vertical structures of the disks, which are shown in Figure 9. The shapes of vertical density profiles are very similar to those produced in local shearing box simulations of radiation pressure dominated accretion disks (Hirose et al. 2009; Jiang et al. 2016b), although the density scale height can be quite different. Consistent with the space-time diagram shown in Figure 2, the density is more centrally concentrated in AGNB52 with a smaller density scale height than the AGN33 run, although the midplane radiation pressure is larger in AGNB52 corresponding to the higher accretion rate. Within  $\sim 45^\circ$  from the disk midplane, density drops by a factor of 250 with height in AGNB52 while it only drops by a factor of 24.5 in AGN33. This is probably caused by the stronger vertically advective cooling due to magnetic buoyancy associated with the MRI dynamo (Jiang et al. 2014a). It also demonstrates that density profiles in radiation pressure dominated accretion disks are determined by the dissipation profiles, not by the hydrostatic equilibrium.

Radiation pressure dominates in the midplane of the disk, but towards the poles magnetic pressure becomes comparable to and then larger than radiation pressure within  $\sim 40^\circ$  from the rotation axis in the run AGNB52. Gas temperature is in thermal equilibrium with the radiation temperature in the disk midplane and hot gas with temperature  $\sim 10^8 K$  is formed in the funnel region. Maxwell stress has two peaks offset from the center by  $10^\circ$  while Reynolds stress peaks at the disk midplane as it follows the density profile. These properties are very similar to the vertical disk structures as studied by local shearing box simulations of MRI turbulence (Miller & Stone 2000; Blaes et al. 2007; Jiang et al. 2014c). For the run AGN33 where magnetic field is not significantly amplified, radiation pressure dominates over the whole disk. Consequently, the gas temperature never increases above  $6 \times 10^5 K$  and there is no hot gas formed in this case (see more discussions in Section 5.4). Reynolds stress is larger than Maxwell stress by a factor of  $\sim 10^5$  at all height. It peaks at the disk midplane and only drops by a factor of  $\sim 4$  at  $45^\circ$  from the disk midplane, which is much smaller compared with the change of density with height. Therefore, dissipation per unit mass due to the Reynolds stress is also larger in the low density regions. However, it does not produce the hot gas easily compared with the case when dissipation in the low density region is dominated by the Maxwell stress. This is probably because dissipation caused by the Reynolds stress happen at the locations of the shocks (see Section 4.5), where density is relatively larger compared with the azimuthally averaged values and the energy can be converted to the photons in a short time scale. Dissipation associated with the Maxwell stress usually happens at locations where magnetic energy is larger and density is smaller than the azimuthally averaged values. Therefore,

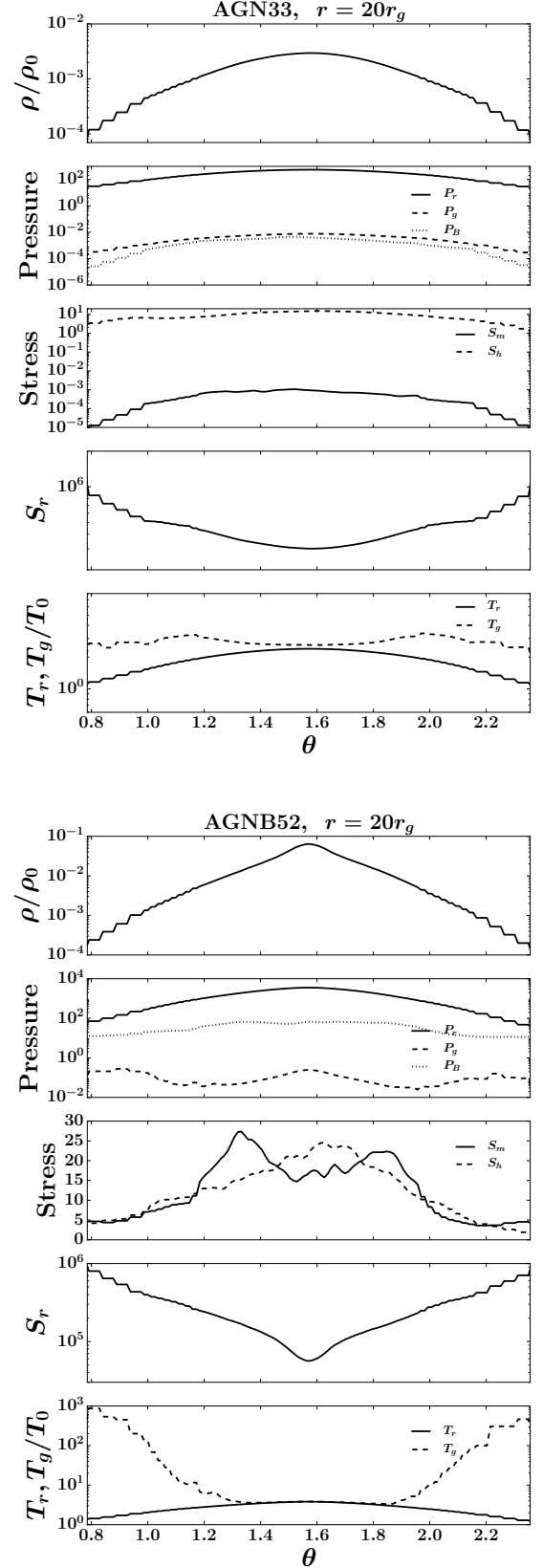


**Figure 9.** Time and shell averaged vertical profiles of various quantities at radius  $20r_g$  for the two runs AGN33 (the top subplot) and AGNB52 (the bottom subplot). From top to bottom panels of each plot, they are density  $\rho$ , gas ( $P_g$ ), radiation ( $P_r$ ) and magnetic ( $P_B$ ) pressure, Reynolds ( $S_h$ ) and Maxwell ( $S_m$ ) stresses, radiation entropy ( $S_r$ ), gas ( $T_g$ ) and radiation ( $T_r$ ) temperatures. All the variables are scaled in the units listed in Table 1 and the unit for radiation entropy is  $P_0/(\rho_0 T_0)$ .

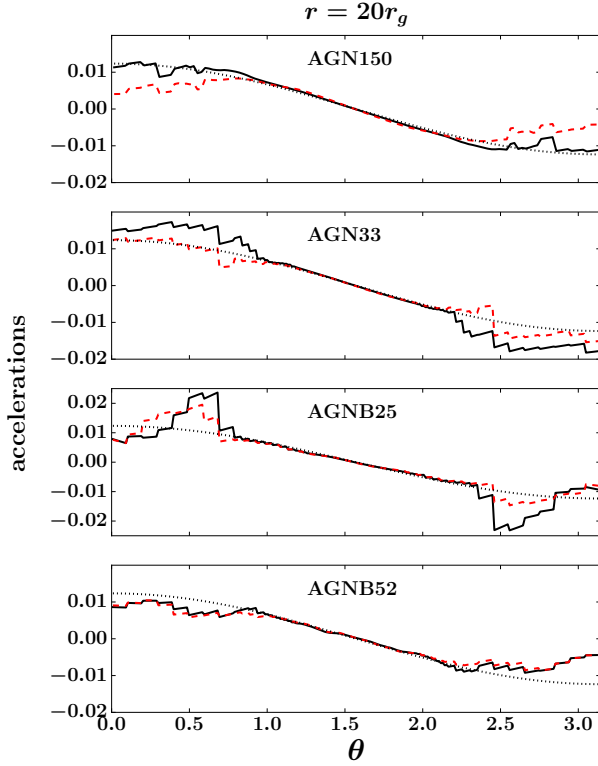


**Figure 10.** Time and shell averaged vertical profiles of the vertical components of radiation accelerations at radius  $20r_g$  compared with the gravitational accelerations for the four simulations. The solid black lines are the volume averaged radiation accelerations  $a_r$  while the dashed red lines are the density weighted radiation accelerations (section 4.4). The dotted black lines are the corresponding vertical component of gravitational accelerations. All these accelerations are scaled with  $c^2/r_g$ .

gas can be heated up without cooling easily.

Vertical profiles of radiation entropy  $S_r = 4E_r/(3\rho T_r)$  for the two runs are shown in the fourth panels of Figure 9, which is the dominant entropy in the strongly radiation pressure dominated regime. Because radiation energy density decreases slower with height compared with density,  $S_r$  always increases with height. This suggests that these strongly radiation pressure dominated disks are stable to the thermally driven convection for both Reynolds stress and Maxwell stress dominated cases, in contrast to the previous suggestions that convection may happen in this regime if dissipation per unit mass is assumed to be a constant (Shakura et al. 1978; Agol et al. 2001; Zhu & Narayan 2013).

Because the dynamic time scale is much shorter than the thermal time scale, we expect the vertical hydrostatic equilibrium to be maintained in the main body of the disk, which is checked at  $20r_g$  for the four runs in Figure 10. As radiation pressure is significantly larger than gas and magnetic pressure in the four runs, we focus on the comparison between radiation and gravitational acceleration. The volume averaged vertical component of radiation acceleration at each  $\theta$  is calculated as  $a_r = \langle \langle \kappa_{aR} + \kappa_s \rangle \rangle (\langle \langle F_{r,r} \rangle \rangle \cos \theta - \langle \langle F_{r,\theta} \rangle \rangle \sin \theta) / c$ , where  $F_{r,r}$  and  $F_{r,\theta}$  are the radial and poloidal components of radiation flux. For turbulent flow with large density fluctuations, more photons can go through the low density regions and cause an anti-correlation between

density and radiation flux fluctuations<sup>1</sup> works to reduce the effective radiation acceleration. This effect can be shown by comparing  $a_r$  with the density weighted radiation acceleration  $a_{r,\rho}$ , which is calculated as  $a_{r,\rho} = \langle \langle \rho (\kappa_{aR} + \kappa_s) (F_{r,r} \cos \theta - F_{r,\theta} \sin \theta) \rangle \rangle / (c \langle \langle \rho \rangle \rangle)$ . The vertical component of gravitational acceleration is  $a_g = GM_{\text{BH}} \cos \theta / (r - 2r_g)^2$ . These accelerations are compared in Figure 10. In the main body of the disks (within  $\sim 30^\circ$  from the disk midplane), gravitational acceleration is balanced by the radiation acceleration, which confirms that the disk is in hydrostatic equilibrium. The density weighted radiation acceleration is also the same as the volume averaged radiation acceleration in the optically thick part of the disk for all the four runs, which is consistent with the results found in Jiang et al. (2015). Above and below the disk midplane,  $a_r$  generally becomes larger than  $a_{r,\rho}$  due to the density fluctuations. For the run AGN150, although  $a_r \sim a_g$  in the funnel regions,  $a_{r,\rho}$  is actually smaller than  $a_g$ , which is consistent with the inflow gas at  $20r_g$  shown in Figure 5. For the run AGN33 and AGNB25,  $a_{r,\rho}$  is slightly larger than the gravitational acceleration consistent with the launching of radiation driven outflow in this region (Figure 5). For the run AGNB52, radiation acceleration is smaller than the gravitational acceleration in the funnel regime and magnetic fields provide additional support to gravity, because magnetic energy density is larger than the radiation energy density in this region.

#### 4.5. Angular Momentum Transfer Caused by the Density Waves

In the previous section, we have shown that the relative contribution of Reynolds stress and Maxwell stress to the angular momentum transfer in the disk can be quite different for the simulations, depending strongly on the net poloidal magnetic flux present in the flow. Contrary to all previous work on MRI driven accretion flows, the Reynolds stress exceeds the Maxwell stress and dominates angular momentum transfer. In this section, we will first show that in all situations, the simulations self-consistently conserve the angular momentum in the disk. Then we will show that the dominant Reynolds stress is consistent with the properties of the spiral shocks formed in the simulations.

##### 4.5.1. The Angular Momentum Flux

Evolution of the sum of gas and radiation momentum is determined by the following equation

$$\frac{\partial}{\partial t} \left( \rho \mathbf{v} + \frac{\mathbf{F}_r}{c^2} \right) + \nabla \cdot (\rho \mathbf{v} \mathbf{v} - \mathbf{B} \mathbf{B} + \mathbf{P}^* + \mathbf{P}_r) = -\rho \nabla \phi. \quad (9)$$

We multiply the above equation with the radial vector  $\mathbf{r}$  and get the evolution equation for the  $z$  component of the angular momentum due to the radial angular momentum transport as

$$\frac{\partial r \sin \theta \rho v_\phi}{\partial t} + \frac{1}{r^2} \frac{\partial}{\partial r} (r^2 F_J) = 0. \quad (10)$$

<sup>1</sup> This is often referred to as “porosity” in the massive star literature (Jiang et al. 2015).

Here  $F_J$  is the radial angular momentum flux

$$F_J \equiv r \sin \theta (\rho v_r v_\phi - B_r B_\phi + P_{r,\phi}), \quad (11)$$

where  $P_{r,\phi}$  is the  $r - \phi$  component of the radiation pressure tensor. Here we only consider angular momentum flux along radial direction. Because gravity is provided by the central point source in the simulations, only the local Reynolds, Maxwell and radiation stresses will provide angular momentum transfer at each radius. We also neglect the term  $\mathbf{F}_r/c^2$  as radiation momentum is usually much smaller than the momentum of the gas.

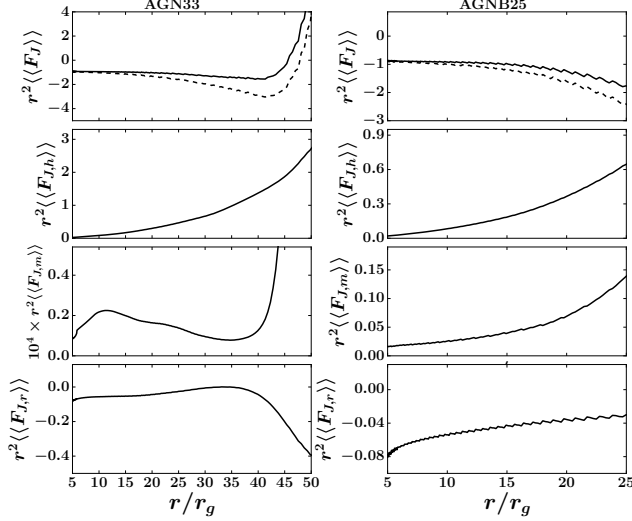


**Figure 11.** Radial profiles of the time and azimuthally averaged total angular momentum flux  $r^2 F_J$  (solid lines in the top panel), angular momentum flux due to Reynolds stress  $r^2 F_{J,h}$  (the second panels), Maxwell stress  $r^2 F_{J,m}$  (the third panels) and radiation stress (the fourth panel). The dashed lines in the top panels are the mean angular momentum flux carried by the net mass flux  $r^2 \langle \langle v_r \rangle \rangle \langle \langle v_\phi \rangle \rangle$ . The left column is for the run AGN33 while the right column is for the run AGNB25. Units of the angular momentum flux  $F_J, F_{J,h}, F_{J,m}$  are all  $r_g P_0$ .

The hydrodynamic stress can be decomposed to the mean and fluctuation components

$$\rho v_r v_\phi = (\delta \rho v_r + \langle \langle \rho v_r \rangle \rangle) (\delta v_\phi + \langle \langle v_\phi \rangle \rangle), \quad (12)$$

where the fluctuation quantities are defined as  $\delta \rho v_r \equiv \rho v_r - \langle \langle \rho v_r \rangle \rangle$ ,  $\delta v_\phi \equiv v_\phi - \langle \langle v_\phi \rangle \rangle$ . The mean hydrodynamic stress is then the sum of the mean Reynolds stress and the angular momentum carried by the mean accretion flow

$$\langle \langle \rho v_r v_\phi \rangle \rangle = \langle \langle \delta \rho v_r \delta v_\phi \rangle \rangle + \langle \langle \rho v_r \rangle \rangle \langle \langle v_\phi \rangle \rangle. \quad (13)$$

In steady state, conservation of angular momentum requires that the time and azimuthally averaged total angular momentum flux  $r^2 \langle \langle F_J \rangle \rangle$  is independent of radius  $r$ , which is checked in Figure 11 for the two runs AGN33 and AGNB25. The contributions of angular momentum flux by the Reynolds stress  $F_{J,h} \equiv r \sin \theta \delta \rho v_r \delta v_\phi$ , Maxwell stress  $F_{J,m} \equiv -r \sin \theta B_r B_\phi$  and radiation stress  $F_{J,r} = r \sin \theta P_{r,\phi}$  are also shown in this Figure. Inside  $\sim 40 r_g$  for the run AGN33 and  $\sim 20 r_g$  for AGNB25,  $r^2 \langle \langle F_J \rangle \rangle$  is indeed roughly a constant. Deviations in larger radii are because the simulations are not run long

enough to reach steady state there. In run AGN33, angular momentum transport is dominated by the Reynolds stress, while Maxwell stress is completely negligible. As shown in Section 4.3, the radiation contribution  $F_{J,r}$  is dominated by the drag of photons due to the mean rotation and inflow of the gas in the disk. The situation is very similar for the run AGN150. For run AGNB25 with net poloidal magnetic fields, angular momentum flux caused by the Maxwell stress is significantly increased and it is only a factor of  $\sim 4$  smaller than the Reynolds stress. When the net poloidal magnetic flux is significantly increased in AGNB52, the Maxwell stress becomes the dominant angular momentum transfer mechanism.

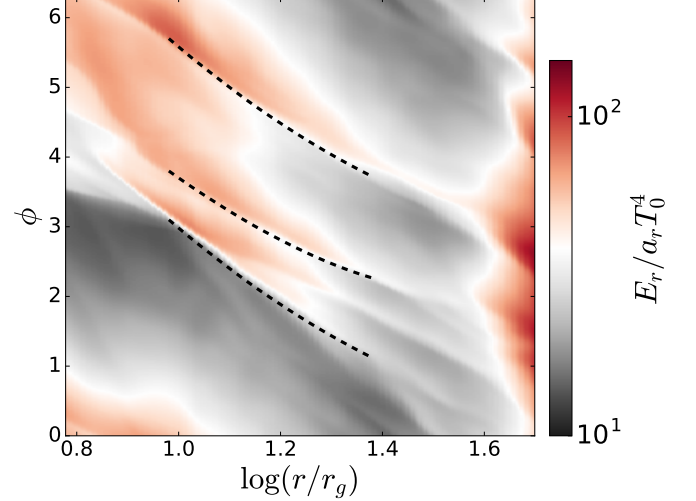


**Figure 12.** Radial and azimuthal distribution of the volume-averaged radiation energy density at the time  $2.77 \times 10^4 r_g/c$  for the simulation AGN33. The volume average is only done within  $30^\circ$  above and below the disk midplane. The three dashed black lines are linear dispersion relations for density waves with pattern speed  $\Omega_p = 2.36 \times 10^{-3} c/r_g$  and wave numbers  $m = 2, 1.5$  and  $2$  respectively (from top to bottom), which fit the locations of shocks very well.

#### 4.5.2. Properties of the Density Waves

To confirm that the spiral structure we see in our simulations (Figure 3) are indeed shocks caused by the density waves, shapes of the spiral structures can be compared with predictions of linear dispersion relation of density waves. Although shocks are clearly nonlinear phenomenon, linear theory can usually do a good job to predict the locations of the shocks (Ju et al. 2016).

To determine the pattern speed of the density waves, at each snapshot, we first take slices of radiation energy density  $E_r$  through the disk midplane. Then we calculate the discrete spatial fourier transform of  $E_r$  over  $\phi$  direction for each radius  $r$ . The spatial fourier power spectra do not show a single value of spatial wavenumber  $m$ . Instead, the spectra are broadly distributed between  $m = 1$  and  $m = 10$  with peaks around  $m = 2$  and  $3$ . The spectra drops significantly with increasing wavenumber when  $m > 10$ . There are more power with larger wavenumber at small radii. For  $r > 20 r_g$ , most of the power is concentrated within  $m < 5$ .

We then take the temporal fourier transform over the snapshots of the real part of the spatial fourier transfer for the  $m = 1$  mode at each radius. The time



intervals for the temporal fourier transfer are chosen to be the same as we use for the time average as described in Section 4.2. Each radius also shows multiple peaks in the temporal fourier transform. However, there is a common peak across different radii, which corresponds to the pattern frequency of the density wave. With this approach, we find the pattern speeds  $\Omega_p$  for the four simulations AGN150, AGN33, AGNB25, AGNB52 are  $1.03 \times 10^{-3}$ ,  $2.36 \times 10^{-3}$ ,  $2.28 \times 10^{-3}$ ,  $1.44 \times 10^{-3} c/r_g$  respectively. These pattern speeds equal Keplerian rotation speeds at 99.4, 57.8, 59.1 and 79.8  $r_g$ . With these pattern speeds, for each spatial wavenumber  $m$ , the linear dispersion relation for density waves describing the relationship between radius  $r$  and azimuthal angle  $\phi$  are (Binney & Tremaine 2008; Ju et al. 2016)

$$d\phi = -\frac{k_r}{m} dr = -\frac{1}{c_{r,s}} \sqrt{(\Omega - \Omega_p)^2 - \kappa^2/m^2} dr. \quad (14)$$

Here  $k_r$  is the radial wavenumber,  $\kappa$  is the epicycle frequency and  $c_{r,s} \equiv \sqrt{4P_r/(3\rho)}$  is the adiabatic radiation sound speed. We have picked the trailing branch of the dispersion relation corresponding to what we see in the simulations. We use the azimuthally averaged  $c_{r,s}$ ,  $\Omega \equiv v_\phi/r$  at each radius in the dispersion relation and  $\kappa$  is taken to be the same as  $\Omega$ . A snapshot of radiation energy density  $E_r$  at time  $2.77 \times 10^4 r_g/c$  averaged within  $30^\circ$  from the disk midplane for simulation AGN33 is shown in Figure 12. There are clearly three shocks between  $8r_g$  and  $31.6r_g$ . We pick three starting points and integrate the dispersion relation to determine the shape of the spiral structures, which are shown as the dashed black lines in Figure 12. If we choose the wavenumber  $m$  to be 2, 1.5 and 2 for the three arms, the dispersion relation can fit the spiral shock positions very well. Notice that we need to choose a non-integer  $m$  value to describe the middle shock, which means that shock is probably formed by merger of multiple linear modes. At each radius along the azimuthal direction, when we cross each shock, density at the shock downstream increases while  $v_\phi$  drops. At the same time, radial inflow velocity develops. This is how the shock driven accretion works. The shock causes the fluid element to lose angular momentum and flow inward. Higher radiation energy density at the shock downstream also means these are the locations where dissipation occurs.

#### 4.5.3. Reynolds Stress due to the Density Waves

Based on the linear analysis of density waves, the amount of Reynolds stress generated by the density waves is proportional to the turbulent radial kinetic energy as (Balbus 2003, Equation 43)

$$\begin{aligned} \langle \langle \delta \rho v_r \delta v_\phi \rangle \rangle &= \frac{m}{rk_r} \left( 1 - \frac{\kappa^2}{m^2 (\Omega - \Omega_p)^2} \right) \langle \langle \rho \delta v_r^2 \rangle \rangle \\ &= \frac{c_{r,s}}{r} \frac{\sqrt{(\Omega - \Omega_p)^2 - \kappa^2/m^2}}{(\Omega - \Omega_p)^2} \langle \langle \rho \delta v_r^2 \rangle \rangle. \end{aligned} \quad (15)$$

Here we calculate the turbulent radial kinetic energy as  $\langle \langle \rho \delta v_r^2 \rangle \rangle = \langle \langle \rho v_r^2 \rangle \rangle - \langle \langle \rho \rangle \rangle \langle \langle v_r \rangle \rangle^2$  and the linear dispersion relation (equation 14) is used to calculate  $m/(rk_r)$ .

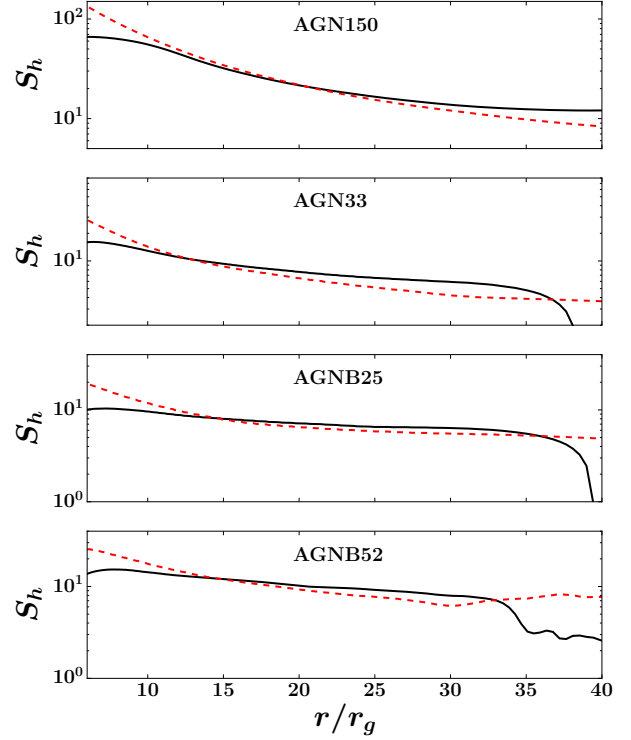


**Figure 13.** Compare the Reynolds stress calculated in the simulations with the predicted values from linear dispersion relations of density waves (equation 15). The dashed red lines are the radial profiles of the time and volume averaged Reynolds stress while the solid black lines are the predicted values with  $m = 2$ . The Reynolds stress we get is comparable to the predicted value.

As multiple modes of density waves are excited in the simulations, we just pick a value of  $m$  to compare the Reynolds stress calculated from the simulations and the predicted stress based on this formula with the pattern speed  $\Omega_p$  we have identified in the last section. The results with  $m = 2$  for the four simulations are shown in Figure 13, which shows that the Reynolds stress given by the linear analysis of density waves is pretty close to what we get from the simulations. The Reynolds stress from  $m = 2$  mode always under-predicts the stress in the inner region ( $r \lesssim 15r_g$ ) and over-predicts the stress in the outer region ( $r \gtrsim 15r_g$ ). This is consistent with what we find in the last section that there are more high wavenumber modes in the small radii and more low wavenumber modes in the large radii.

#### 4.6. Properties of the Emerging Photons and Outflow

Outflow coming from the funnel region of the disk along the rotation axis is a natural outcome of the accretion disks with accretion rates above the Eddington limit. That is also the region where most of the photons escape. Shape of the funnel region can be quantified by the location where total optical depth measured from the rotation axis  $\tau_R$  reaches one, which is calculated as

$$\tau_R = \int_0^R (\kappa_s + \kappa_a R) \rho dR. \quad (16)$$

This is shown as the dashed black lines in Figure 5. Because of the mesh structure and logarithmic grid we use,



the funnel is better resolved near the disk midplane and poorly resolved at larger radius. For simulation AGN150 with  $\dot{M} = 150\dot{M}_{\text{Edd}}$ , almost all the funnel region becomes optically thick. Particularly, the outflow only develops from  $\sim 50r_g$ . For the other runs, the outflow starts  $\sim 10r_g$ . The optically thin part of the funnel is also small in AGNB52 because density drops very slowly with height due to strong magnetic pressure and the net accretion rate is also larger than the values in AGN33 and AGN150. Radiation energy density and radiation flux streamlines ( $F_{r,r}$  and  $F_{r,\theta}$  components only) for the two runs AGN33 and AGNB25 are shown in Figure 14, which also shows the ratio between radiation flux magnitude and  $cE_r$ . This figure shows the large scale structures of the radiation flux within  $800r_g$  in height as well as the inner region of the disks within  $100r_g$ . The ratio  $|\mathbf{F}_r|/(cE_r)$  is almost zero near the optically thick midplane and reaches  $\sim 0.4$  at  $r \sim 200r_g$ . Most of the photons leaving in the outflow region can trace back to the inner  $\sim 40r_g$  with streamlines nearly parallel to the rotation axis. When  $r \gtrsim 200r_g$ , the angle between rotation axis and radiation flux increases as density from the disk drops and it is not optically thick enough to collimate the photons.

To calculate the total radiative and kinetic energy luminosity carried with the outflow, we use the fluxes through a cylindrical surface of radius  $R_0 \sim 30 - 40r_g$ . We use this surface rather than the radial boundary of our simulation domain because the radiation and outflow through this surface is driven primarily by the accretion in the inner  $30-40r_g$ , where our simulations have reached a steady state. If we extended this surface further out, it would start to encompass regions where the emission and outflow are dominated by the still relaxing portions of our initial torus. We first convert the azimuthally averaged flow velocity  $\mathbf{v}$ , mass flux  $\rho\mathbf{v}$  and radiation flux  $\mathbf{F}_r$  from  $r, \theta$  plane in the spherical polar coordinate system to the  $R, z$  plane in the cylindrical coordinate. Then the total radiative luminosity  $L_r$ , kinetic energy luminosity  $L_k$  and mass flux  $\dot{M}_w$  leaving from a fixed height  $z$  inside the cylindrical radius  $R_0$  are calculated as

$$\begin{aligned} L_r &= \int_0^{R_0} 2\pi F_{r,z} R dR + \int_{-z}^z 2\pi R_0 F_{r,R} dz, \\ L_k &= \int_0^{R_0} 2\pi v_z \left( \frac{1}{2} \rho v^2 \right) R dR \\ &\quad + \int_{-z}^z 2\pi v_R \left( \frac{1}{2} \rho v^2 \right) R_0 dz, \\ \dot{M}_w &= \int_0^{R_0} 2\pi \rho v_z R dR + \int_{-z}^z 2\pi \rho v_R R_0 dz. \end{aligned} \quad (17)$$

We sum contributions from both sides of the disk. For the integral along the cylindrical surface at the fixed radius  $R_0$ , we only include regions with positive  $F_{r,R}$  and  $v_R$  to exclude the inflow part in the main body of the disk. For  $L_k$  and  $\dot{M}_w$ , we only include fluid elements when the sum of kinetic and gravitational potential energies are positive, which indicates that the gas is truly unbound. The time averaged values of  $L_r, L_k$  are calculated during the time period as specified in Section 4.2.

Vertical profiles of  $L_r$  and  $L_k$  for the two runs AGN33

and AGNB25 are shown in Figure 15. We choose  $R_0 = 40r_g$  for AGN33 and  $R_0 = 30r_g$  for AGNB25 to match the steady state part of the disk in the simulations. The radiative and kinetic luminosities increase rapidly inside  $100r_g$  and  $L_r$  reaches a roughly constant value beyond  $z \approx 400r_g$ , which is  $16.6L_{\text{Edd}}$  for AGN33 and  $18.4L_{\text{Edd}}$  for AGNB25 respectively. The kinetic luminosity  $L_k$  also saturates to  $5.6L_{\text{Edd}}$  for AGN33 and  $2.7L_{\text{Edd}}$  for AGNB25 near the boundary of our simulation domain. This demonstrates that our simulation domain is large enough to capture the energy exchange between the photons and gas. The kinetic luminosity is only 34% and 15% of the radiative luminosity in the two simulations. As the net mass accretion rate is  $33\dot{M}_{\text{Edd}}$  inside  $40r_g$  for AGN33 and  $25\dot{M}_{\text{Edd}}$  inside  $30r_g$  for the two runs respectively, the radiative efficiencies are 5.0% and 7.3%, which are comparable to the value we get in Jiang et al. (2014a).

Although Figure 7 shows that there is a significant fraction of gas moving outward in the disk, not all of them are unbound outflow. At the outer boundary of our simulation domain, mass fluxes associated with the gas which has kinetic energy larger than the gravitational energy are  $18.1\dot{M}_{\text{Edd}}$  for AGN33 and  $8.1\dot{M}_{\text{Edd}}$  for AGNB25, which are 54.8% and 32.4% of the net mass accretion rates.

For the run AGN150, outflow only starts around  $50r_g$ , inside which all the photons are advected towards the black hole. The outflow velocity at the outer edge of the simulation box is smaller by a factor of  $\sim 2$  compared with the corresponding values in AGN33 and AGNB25. Although the outer edge of the simulation box is still very optically thick,  $L_r$  shows similar properties as in Figure 15, which reaches a constant value beyond  $z = 1200r_g$ . This can happen in the optically thick region because most of the luminosity comes from the advection of the photons while radiative acceleration associated with the co-moving frame flux roughly balances the gravitational acceleration. Therefore the gas is not accelerated and radiation energy is not converted to the gas kinetic energy. At the boundary of the simulation domain,  $L_r = 15.5L_{\text{Edd}}$  while  $L_k = 3.6L_{\text{Edd}}$ . As the net mass accretion rate is  $150\dot{M}_{\text{Edd}}$ , the radiative efficiency is only 1%. The mass flux associated with the unbound outflow is  $23\dot{M}_{\text{Edd}}$ , which is 15% of the net mass accretion rate.

Because of the limited radial range we can reach steady state for the run AGNB52, we will not try to estimate the radiative efficiency for this run, as we will likely miss a lot of radiation flux at larger radii. Although the optical depth in the funnel region is larger in this run compared with AGN33 and AGNB25, outflow starts around  $20r_g$ , which is much smaller compared with the run AGN150. Therefore, we expect the radiative efficiency in AGNB52 to be larger than the value in AGN150, but smaller than the values in AGN33 and AGNB25.

#### 4.7. Energy Transport Mechanisms in the Disk

The energy dissipated in the main body of the disk needs to be transported to the funnel region efficiently before the photons are advected to the black hole in order to achieve relatively large radiative efficiency compared to the values predicted by the slim disk model. Jiang

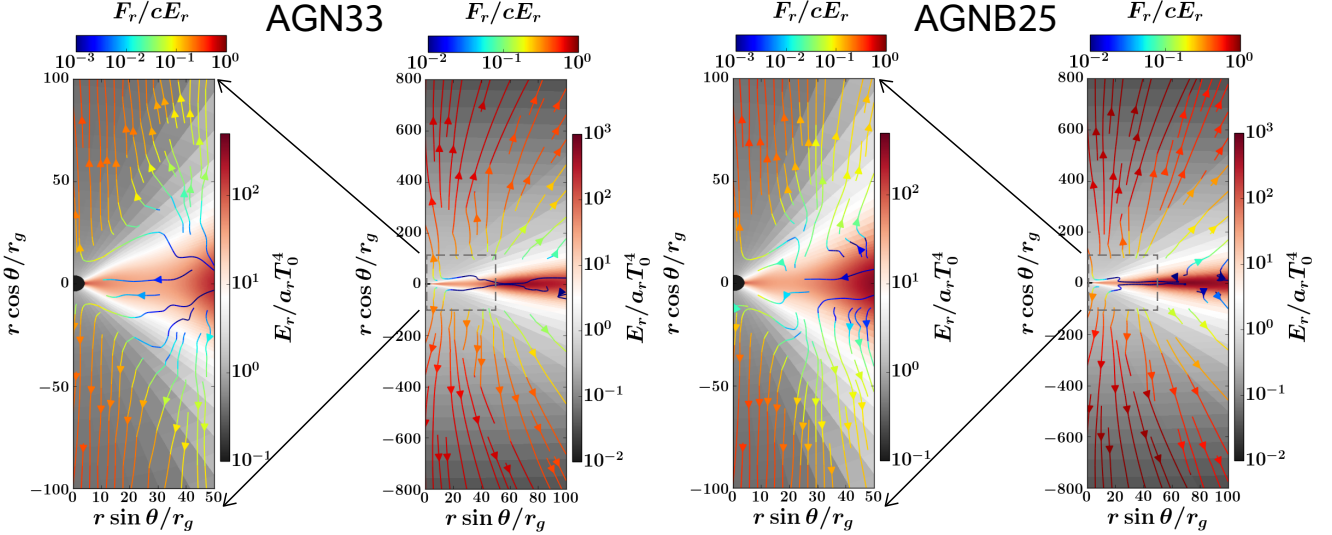


**Figure 14.** Time and azimuthally averaged spatial structures of radiation energy density  $E_r$  (colors) and radiation flux  $\mathbf{F}_r$  (streamlines, only includes the azimuthally averaged  $r, \theta$  components  $F_{r,r}$ ,  $F_{r,\theta}$ ). Color of the streamlines is the ratio  $|\mathbf{F}_r|/(cE_r)$ . The left two panels are for the run AGN33 while the right two panels are for the run AGNB25. In each case, the first panel shows the inner structures with height smaller than  $100r_g$  while the second panel show the disk structures up to  $800r_g$  in height.

et al. (2014a) shows that magnetic buoyancy allows photons to move vertically with a speed (typically the local Alfvén speed (e.g., Stella & Rosner 1984; Jiang et al. 2016a)) much larger than the photon diffusion speed in the super-Eddington accretion regime. The signature for this mechanism to be working is the strong anti-correlation between the azimuthal fluctuations of density and magnetic energy density (Blaes et al. 2011; Jiang et al. 2014a). Time averaged cross correlation coefficients  $\sigma_{\rho, P_B}$  between  $\rho$  and  $P_B$  for the four runs are shown in Figure 16. Density and magnetic pressure fluctuations are actually correlated in AGN150 and AGN33. They become anti-correlated in the main body of the disks in AGNB25 and AGNB52. This is because in the two runs AGN150 and AGN33 when there are no net vertical magnetic fields, Maxwell stress is weak and magnetic pressure is smaller than the radiation pressure by  $\sim 10^3 - 10^4$  (Figure 8). While in the two runs AGNB25 and AGNB52 with net vertical magnetic fields, magnetic fields are significantly amplified and magnetic pressure can reach  $\sim 10\%$  of radiation pressure. In order for the magnetic buoyancy to work, azimuthal fluctuations of magnetic pressure in the low density region should be able to balance fluctuations of gas and radiation pressure in the high density regions, which cannot happen for AGN150 and AGN33 as magnetic pressure is too small.

As discussed in last section, even magnetic buoyancy is not working in AGN33, the radiative efficiency is comparable to the values in AGNB25. This is because when accretion is driven by the density waves, the Reynolds stress decreases with height much slower compared with the density profile (Figure 9). This means a significant fraction of dissipation happens in the low density regions, where the photon diffusion time is small. As long as the funnel region is not very optically thick, these photons can escape with the outflow. While in run AGN150 where the funnel becomes optically thick and all the dissipation is still very far away from the outflow region, radiative efficiency drops significantly.

## 5. DISCUSSION

### 5.1. Excitation Mechanism of the Spiral Density Waves

Based on our analysis in Section 4.5, the spiral density waves are clearly responsible for the large Reynolds stress we find from the simulations. However, it is still unclear physically what sets the pattern speed of the global density waves in the simulations. In section 4.5.2, we have determined that the pattern speeds of the density waves in the four simulations correspond to the Keplerian rotation velocity at radii varying from 57 to  $100r_g$ . We have also checked that there are no special asymmetrical structures at these radii that may be responsible for the excitation of density waves. The initial tori in these simulations have the same shape and are centered at the same radii for the three runs AGN150, AGN33 and AGNB25 but pattern speeds in the three runs correspond to the orbital rotation speed at quite different radii. The run AGNB52 has the initial torus closer to the central black hole but its pattern speed is smaller than the values in AGN33 and AGNB25. These results are inconsistent with excitation of density waves by some special structure(s) in the initial torus region. Instead, it seems that the density waves are self-excited within the inner accretion flow itself.

Excitation of density waves is very common in accretion disks. In binary systems with the gravitational force from the companion star providing the perturbing force in the disks, the pattern speed of density waves can be easily associated with the orbital speed of the companion (Shu & Lubow 1981; Papaloizou & Lin 1995; Ju et al. 2016). Spiral density waves can also be excited without a perturbation at a fixed location, although density waves in this case may not be very coherent and less prominent compared with the previous case. For example, density waves are commonly observed in disks with self-gravitational instability (Dong et al. 2015; Kratter & Lodato 2016), which also do not have a particular perturber at a fixed radius that may correspond to the pattern speed of the density waves. Turbulence from MRI can also excite spiral density waves (Heinemann & Pa-

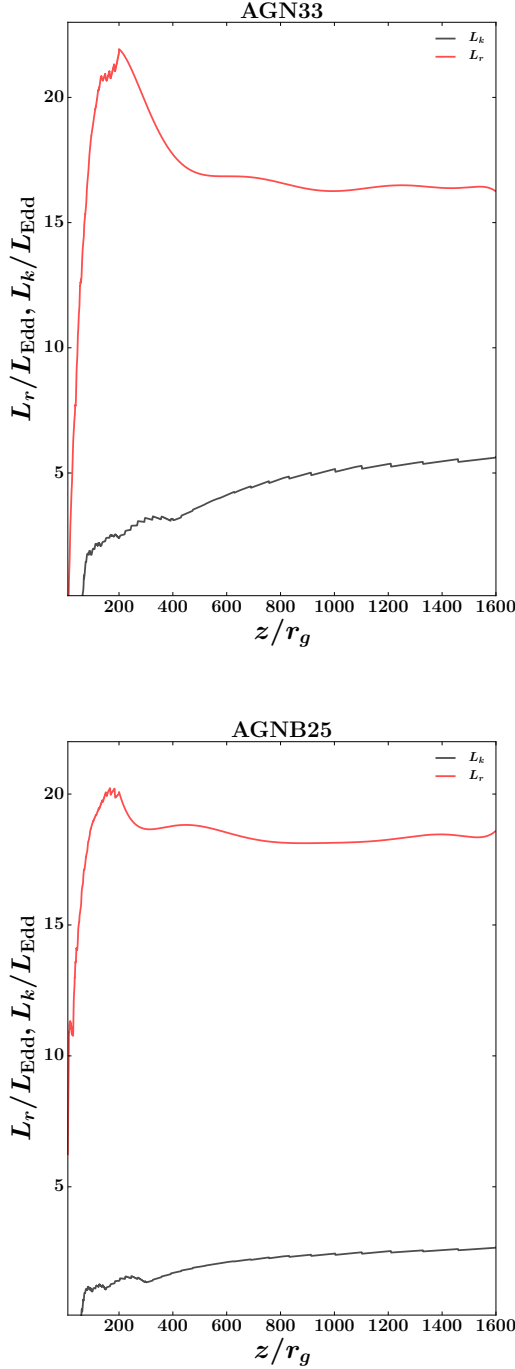


**Figure 15.** Vertical profiles of total radiative luminosity ( $L_r$ , red lines) and kinetic luminosity associated with the unbound outflow ( $L_k$ , black lines) for the simulations AGN33 (top panel) and AGNB25 (bottom panel). The luminosities are calculated through the surface of cylinders with radii  $R = 40r_g$  and  $R = 30r_g$  for the two runs AGN33 and AGNB25 respectively. Both  $L_r$  and  $L_k$  reach roughly constant values with height near the boundary of our simulation domain and  $L_r$  is significantly larger than  $L_k$  in the simulations. We have smoothed the curves of  $L_r$  to remove the oscillations due to the coarse grid at large radii.

paloizou 2009a,b), which may explain how the density waves are excited in our simulations. However, it is unclear how the density waves excited at different radii form a coherent structure globally, which strongly motivates further study of this issue in future work.

It is well known that the propagation of density waves depends on the Mach number of the disk (Savonije et al. 1994; Ju et al. 2016, 2017), which is related to the ratio between the disk scale height and radius. In the super-Eddington accretion disks, the disk is thicker and density waves have longer wavelength. These spiral density waves propagate further and more efficiently transport angular momentum. For AGN disks with sub-Eddington accretion rates, the disk is thinner and Mach number will increase. Even if density waves are also excited there, they may have difficulty propagating. The role of density waves in these lower accretion rate disks will be a topic of future study.

### 5.2. Angular Momentum Transfer with the Radiation Field

In the optically thick regime, radiating fluid in the co-moving frame can be described as a viscous gas with radiation providing the shearing viscosity (Mihalas & Mihalas 1984; Kaufman & Blaes 2016) as (in the spherical polar coordinate)

$$P_{r,vis}^{r,\phi} = \frac{8}{27} \frac{E_{r,0}}{\rho c^2} \frac{c}{\kappa_t} \left[ \frac{1}{r \sin \theta} \frac{\partial v_r}{\partial \phi} + r \frac{\partial}{\partial r} \left( \frac{v_\phi}{r} \right) \right], \quad (18)$$

where  $E_{r,0}$  is the radiation energy density in the co-moving frame and  $\kappa_t \equiv \kappa_s + \kappa_{aR}$  is the total Rosseland mean opacity. Compared with radiation pressure, radiation viscosity is the order of  $\mathcal{O}(\lambda_p v_\phi / rc)$  with  $\lambda_p$  to be the photon mean free path across radius  $r$ . Radiation viscosity depends on the velocity gradient and can in principle transfer angular momentum outward along with the Maxwell stress and Reynolds stress. However, this is different from the off-diagonal component of the lab frame radiation pressure  $P_r^{r,\phi}$  in the total angular momentum flux equation 10, which is related to the co-moving frame radiation pressure  $P_{r,0}$  as given by equation 91.12 of Mihalas & Mihalas (1984). Even with isotropic radiation field in the co-moving frame,  $P_r^{r,\phi}$  still has a component proportional to the velocity as (to the order of  $\mathcal{O}(v/c)^2$ )

$$P_r^{r,\phi} \approx \frac{4}{3} \frac{v_r v_\phi}{c^2} E_{r,0}, \quad (19)$$

which is non-zero for the disk with inflow  $v_r$  and rotation  $v_\phi$ . Physically, this term multiplied by  $r \sin \theta$  represents the angular momentum flux in the radiation field carried with the accretion flow, which is smaller than the hydrodynamic component  $\rho v_r v_\phi$  by a factor of  $E_{r,0}/\rho c^2$ . When we estimate the *outward* angular momentum flux caused by the radiation field in Section 4.3, we need to subtract the *inward* component associated with  $\langle \langle \rho v_r \rangle \rangle$  and  $\langle \langle v_\phi \rangle \rangle$ . This is similar to what we have done to determine the contribution of outward angular momentum transport due to the Reynolds stress.

Because of the large optical depth in the super-Eddington accretion disks,  $P_r^{r,\phi}$  is dominated by the component associated with the inflow gas, while radiation viscosity is much smaller than the Maxwell stress

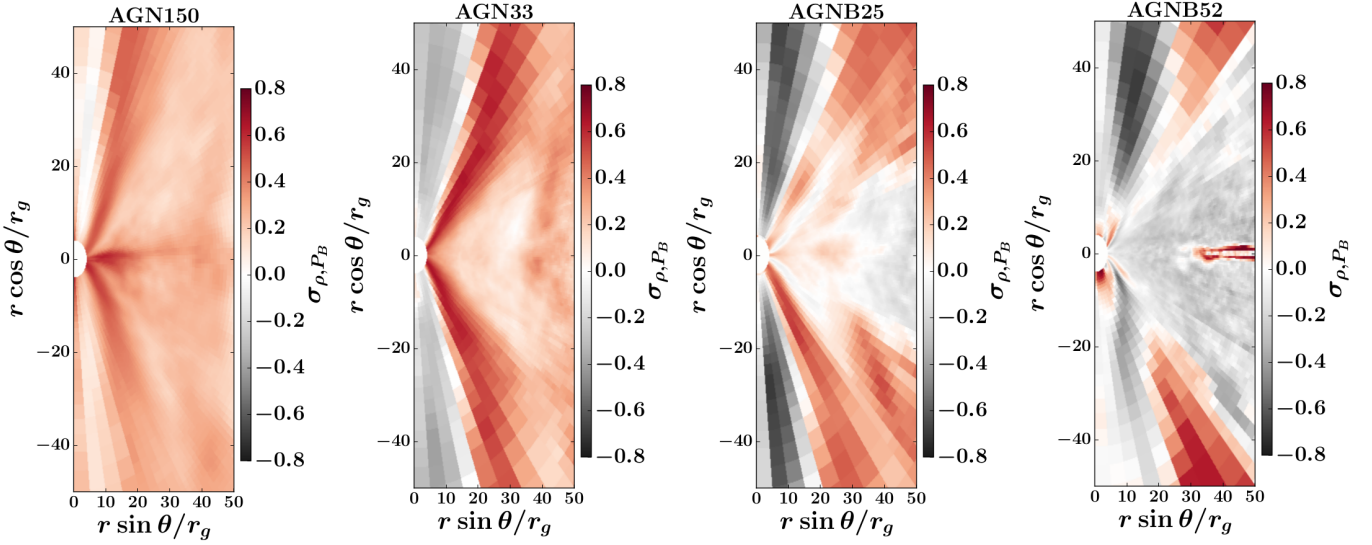


**Figure 16.** Time averaged cross correlation coefficients  $\sigma_{\rho, P_B}$  between azimuthal density and magnetic pressure fluctuations for the four runs in the inner regions of the disks. Positive correlations are found for AGN150 and AGN33 where magnetic pressure is much smaller than the radiation pressure. In AGNB25 and AGNB52 where Maxwell stress provides a significant fraction of the total stress, negative cross correlations between  $\rho$  and  $P_B$  show up.

and Reynolds stress as shown in Figure 8. When accretion rate drops to the sub-Eddington regime the optical depth is expected to drop, increasing the photon mean free path. At the same time, the radiation pressure to gas pressure ratio will decrease. The former increases the importance of radiation viscosity while the latter decreases it. If the increased mean free path is more important, than radiation viscosity may play a larger role in angular momentum transport in the sub-Eddington flows, a topic we will examine in future study.

### 5.3. Comparison with super-Eddington Accretion Disks around Stellar Mass Black Holes

The simulations presented here represent the first radiation magneto-hydrodynamics study of super-Eddington accretion onto supermassive black holes with realistic parameters. Many properties of these disks are unique outcome of the extremely large ratio between radiation pressure and gas pressure, which cannot happen for simulations designed for stellar mass black holes.

The significant Reynolds stress (comparable or even larger than the Maxwell stress) caused by the spiral shocks found in these AGN simulations is not observed for the stellar mass black hole case Jiang et al. (2014a). This is also true for simulations designed for stellar mass black holes done by many other groups (Ohsuga et al. 2005; McKinney et al. 2014; Sądowski et al. 2014). The large radiation pressure is likely responsible for the suppression of Maxwell stress as well as the enhanced Reynolds stress because of the increased compressibility of the flow in this regime. For a similar net mass accretion rate in Eddington unit, the AGN disks have much larger turbulent inflow and outflow mass fluxes compared with the disks around stellar mass black holes. This can be confirmed by comparing the run AGNB52 at the bottom panel of Figure 7 and Figure 4 of Jiang et al. (2014a). The mass flux as well as the kinetic energy flux associated with the unbound outflow in the AGN disks are also larger than the values in disks around stellar mass black holes.

Despite the above differences, many properties of the super-Eddington accretion disks are common for both AGNs and stellar mass black holes. They both show strong radiation driven outflow along the funnel region with similar escaping velocity  $\sim 0.3c - 0.4c$  for disks with similar net mass accretion rate in Eddington unit. When the accretion rates are  $\sim 25 - 50\dot{M}_{\text{Edd}}$ , these simulations do confirm that the radiative efficiency can reach  $\sim 4\% - 6\%$  as in Jiang et al. (2014a), although it is still unclear why it is different from the results found by others (McKinney et al. 2014; Sądowski et al. 2014) in the similar accretion rate range. In the case when MRI turbulence is the dominant mechanism for angular momentum transfer, we also see the butterfly diagram as well as the vertical advective cooling due to magnetic buoyancy as in Jiang et al. (2014a). When accretion rate reaches  $150\dot{M}_{\text{Edd}}$ , the radiative efficiency drops significantly as suggested in the slim disk model. The differences are clearly shown in Figure 5. In this case, most of the funnel region becomes optically thick. The disk has inflow instead of outflow inside  $\sim 50 - 60r_g$ . As most of the dissipation still happens in this region, the photons are trapped and advected towards the black hole with a small fraction radiated due to the diffusive flux.

### 5.4. Observational Implications for Super-Eddington Accretion disk in AGNs

Mid-plane temperatures of these super-Eddington AGN disks vary from  $\sim 4 \times 10^5 K$  to  $8 \times 10^5 K$ , which are much smaller than the temperature of disks around stellar mass black holes. This is consistent with the standard disk models (Shakura & Sunyaev 1973; Abramowicz et al. 1980). However, the optically thick outflow in the super-Eddington regime pushes the photosphere away from the disks, which reduces the effective temperature. The super-Eddington luminosity is achieved with larger emission area and smaller effective temperature compared with the standard disk models, which will likely change the observational appearance of these

disks. Although we do not have theoretically calculated spectra for these disks yet, the effective temperature of the radiation field calculated by the simulations can give us an order of magnitude estimate of the expected spectrum peaks. For the runs AGN150, AGN33, AGNB25, AGNB52, at the fixed height  $z = 1600r_g$ , the radiation temperatures  $T_r$  are  $\sim 9.6 \times 10^4 K$ ,  $5.0 \times 10^4 K$ ,  $8.6 \times 10^4 K$  and  $1.0 \times 10^5 K$  respectively inside  $100r_g$  from the rotation axis. Because density near the outer boundary of the simulation domain for the run AGN150 is still much larger than the density of the other runs, the effective temperature at the true photosphere will likely be even smaller.

The above estimated effective radiation temperature cannot tell us the properties of X-rays from these disks, as X-rays from AGNs are generally believed to be produced by the Compton scattering with hot electrons. As shown in Figure 9, thermal properties of the gas in the funnel regions are quite different for disks primarily driven by spiral shocks or MRI turbulence. This can also be seen clearly in Figure 17, which shows the azimuthally averaged spatial distribution of gas temperature in the four runs. For the runs AGNM1 and AGNM2 with significant spiral density waves and very weak MRI turbulence, the gas is barely heated above  $\sim 10^7 K$ . The gas starts to be heated above  $10^8 K$  in the run AGNB25 with a weak poloidal magnetic field and stronger MRI turbulence. Significant hot gas with temperature up to  $\sim 10^9 K$  shows up in the run AGNB52 with MRI turbulence to be the dominant mechanism for angular momentum transfer. However, despite the differences of gas temperature in the inner region of the disk, they are all embedded within the optically thick outflow in these super-Eddington disks. The total optical depths from the hot gas to the observer with most viewing angles are still much larger than 1. Therefore, we expect X-rays from super-Eddington AGN disks are generally much weaker.

Our super-Eddington accretion disks with accretion rate  $\sim 20 - 50\dot{M}_{\text{Edd}}$  can have total radiative luminosity  $\sim 10 - 20L_{\text{Edd}}$ , which is larger than the luminosity predicted by the slim disk model. However, because of the drop of radiative efficiency with accretion rate  $\sim 150\dot{M}_{\text{Edd}}$ , the radiative luminosity from super-Eddington disks does not increase with increasing mass accretion rate indefinitely. In fact, luminosity from the run AGN150 is smaller than  $10L_{\text{Edd}}$  despite the largest mass accretion rate in the four runs. This implies that after including the advective cooling along the vertical direction and realistic spatial distribution of dissipation, there will still be a maximum luminosity that the super-Eddington accretion disks can have, which is much larger than  $L_{\text{Edd}}$  though.

## 6. SUMMARY

In summary, we have shown four 3D global radiation magneto-hydrodynamic simulations of super-Eddington accretion disks onto a  $5 \times 10^8 M_\odot$  black hole for the first time. The accretion rates reach  $\sim 25$  to  $150\dot{M}_{\text{Edd}}$ , leading to a radiation pressure to gas pressure ratio of  $\sim 10^4 - 10^5$ , which is expected only in AGN disks. The most important results we find from the simulations are summarized below.

- When the accretion rate is  $\sim 25 - 50\dot{M}_{\text{Edd}}$ , outflow is launched along the funnel region starting from  $5 - 10r_g$  with terminal velocity  $\sim 0.3 - 0.4c$ . In this case, the radiative efficiency can reach  $\sim 5 - 7\%$ . The dissipated energy in the main body of the disk can be efficiently advected to the funnel region and carried out by the outflow. The total kinetic energy luminosity associated with the funnel outflow is  $\sim 15 - 30\%$  of the radiative luminosity. Mass flux carried by the outflow varies from  $15\% - 50\%$  of the net mass accretion rate in the disk.
- When the accretion rate reaches  $\sim 150\dot{M}_{\text{Edd}}$ , the optically thin funnel region with respect to the rotation axis is smaller than  $5^\circ$ . Outflow is launched from  $\sim 50 - 70r_g$  with final speed  $\sim 0.1 - 0.15c$ . The radiative efficiency drops below  $1\%$  with luminosity smaller than  $15.5L_{\text{Edd}}$ , because most of the energy is advected towards the black hole in this case. The total kinetic energy luminosity carried with the outflow is  $3.6L_{\text{Edd}}$  while the outflow mass flux is  $\sim 15\%$  of the net mass accretion rate.
- Density waves are excited in the disks when gas flows towards the black hole from the initial torus. These density waves transfer angular momentum via spiral shocks. In the case when there are either no or only small amount of net poloidal magnetic fields, Maxwell stress produced by the MRI turbulence is suppressed in the strongly compressible radiation pressure dominated flow. Reynolds stress generated by the spiral shocks is the dominant mechanism for angular momentum transfer. Maxwell stress only becomes larger than the Reynolds stress when the ratio between radiation pressure and magnetic pressure associated with the mean poloidal magnetic fields  $\langle\langle B_\theta \rangle\rangle^2/2$  is smaller than  $\sim 10^4$ .
- Although radiation pressure is  $\sim 10^4 - 10^6$  times larger than the gas pressure and the radiation sound speed reaches  $\sim 10\%$  speed of light, radiation viscosity plays a very minor role compared with Maxwell and Reynolds stresses for angular momentum transfer in these super-Eddington accretion disks because the large optical depth corresponds to a small mean free path.
- Super-Eddington accretion disks driven by spiral shocks do not produce hot gas in the funnel region. The gas temperature is always smaller than  $\sim 10^7 K$ . For the disk with MRI turbulence being the dominant mechanism for angular momentum transfer, hot gas with temperature up to  $10^9 K$  is observed. However, all the hot gas is covered by the optically thick outflow and super-Eddington AGN disks are expected to be X-ray weak.

There are a few caveats of the simulations that we will improve in the future. We adopt the pseudo-Newtonian potential to mimic the general relativity effects around a non-spinning black hole, which means we cannot follow the formation of relativistic jets by spinning black holes. Extending our radiative transfer scheme to work in general relativity will be our next step. Adding frequency-dependent transport to the existing simulations will also



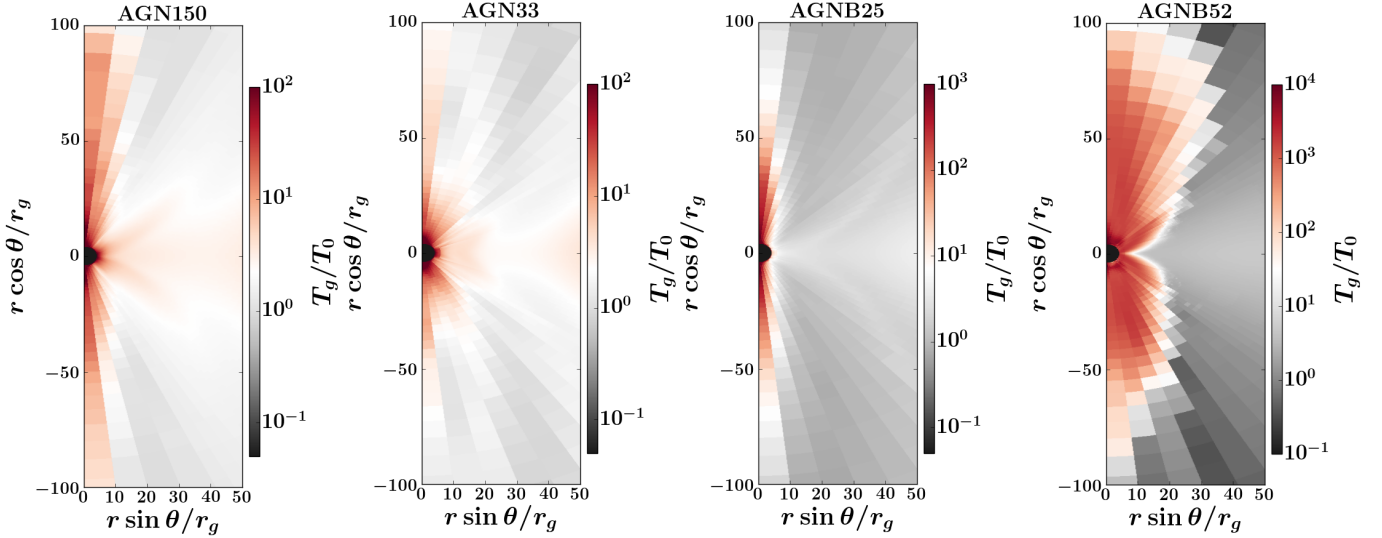


**Figure 17.** Time and azimuthally averaged spatial structures of gas temperature  $T_g$  in unit of  $T_0 = 2 \times 10^5 K$ . From left to right, they are for runs AGN150, AGN33, AGNB25, AGNB52 as labeled in each panel. The disks driven by spiral shocks do not have hot gas with temperature significant above  $10^7 K$  as in AGN150 and AGN33, while AGNB52 shows hot gas with temperature up to  $\sim 10^9 K$ .

be important to handle the Compton scattering self-consistently and treat the frequency dependence of the opacity accurately for AGN disks. The line-driven wind, which is believed to be important to drive the large scale outflows in most AGNs, is also not included in these simulations. It will be interesting to see how important it is for these super-Eddington disks. Lastly, we have started to post-process our simulations to compute synthetic spectra, which will be shown in a separate publication.

#### ACKNOWLEDGEMENTS

We thank Omer Blaes, Geoffroy Lesur, Jeremy Goodman, Charles Gammie, Julian Krolik as well as many participants of the accretion disk program in KITP for helpful discussions. This research was supported in part by the National Science Foundation under Grant No. NSF PHY-1125915 and AST-1333091. S.W.D. is supported by a Sloan Foundation Research Fellowship and a Virginia Space Grant Consortium New Investigator award. An award of computer time was provided by the Innovative and Novel Computational Impact on Theory and Experiment (INCITE) program. This research used resources of the Argonne Leadership Computing Facility, which is a DOE Office of Science User Facility supported under Contract DE-AC02-06CH11357. Resources supporting this work were also provided by the NASA High-End Computing (HEC) Program through the NASA Advanced Supercomputing (NAS) Division at Ames Research Center and the Extreme Science and Engineering Discovery Environment (XSEDE), which is supported by National Science Foundation (NSF) grant No. ACI-1053575.

#### REFERENCES

- Abramowicz, M. A., Calvani, M., & Nobili, L. 1980, *ApJ*, 242, 772  
 Agol, E., Krolik, J., Turner, N. J., & Stone, J. M. 2001, *ApJ*, 558, 543  
 Armitage, P. J. 1998, *ApJ*, 501, L189  
 Bai, X.-N., & Stone, J. M. 2013, *ApJ*, 767, 30  
 Balbus, S. A. 2003, *ARA&A*, 41, 555  
 Balbus, S. A., & Hawley, J. F. 1991, *ApJ*, 376, 214  
 Begelman, M. C., & Volonteri, M. 2017, *MNRAS*, 464, 1102  
 Béthune, W., Lesur, G., & Ferreira, J. 2016, *arXiv:1612.00883*  
 Binney, J., & Tremaine, S. 2008, *Galactic Dynamics: Second Edition* (Princeton University Press)  
 Blackman, E. G. 2012, *arXiv:astro-ph/1203.0823*  
 Blackman, E. G., Penna, R. F., & Varnière, P. 2008, *New Astronomy*, 13, 244  
 Blaes, O., Hirose, S., & Krolik, J. H. 2007, *ApJ*, 664, 1057  
 Blaes, O., Krolik, J. H., Hirose, S., & Shabaltas, N. 2011, *ApJ*, 733, 110  
 Brandenburg, A., Nordlund, A., Stein, R. F., & Torkelson, U. 1995, *ApJ*, 446, 741  
 Ciotti, L., & Ostriker, J. P. 2007, *ApJ*, 665, 1038  
 Ciotti, L., Ostriker, J. P., & Proga, D. 2010, *ApJ*, 717, 708  
 Davis, S. W., Stone, J. M., & Pessah, M. E. 2010, *ApJ*, 713, 52  
 Dong, R., Hall, C., Rice, K., & Chiang, E. 2015, *ApJ*, 812, L32  
 Fromang, S., Latter, H., Lesur, G., & Ogilvie, G. I. 2013, *A&A*, 552, A71  
 Fromang, S., & Lesur, G. 2017, *arXiv:1705.03319*  
 Gardiner, T. A., & Stone, J. M. 2005, in *American Institute of Physics Conference Series*, Vol. 784, *Magnetic Fields in the Universe: From Laboratory and Stars to Primordial Structures*, ed. E. M. de Gouveia dal Pino, G. Lugones, & A. Lazarian, 475–488  
 Guan, X., Gammie, C. F., Simon, J. B., & Johnson, B. M. 2009, *ApJ*, 694, 1010  
 Hawley, J. F. 2001, *ApJ*, 554, 534  
 Hawley, J. F., Gammie, C. F., & Balbus, S. A. 1995, *ApJ*, 440, 742  
 Hawley, J. F., Guan, X., & Krolik, J. H. 2011, *ApJ*, 738, 84  
 Hawley, J. F., Richers, S. A., Guan, X., & Krolik, J. H. 2013, *ApJ*, 772, 102  
 Heinemann, T., & Papaloizou, J. C. B. 2009a, *MNRAS*, 397, 52  
 —. 2009b, *MNRAS*, 397, 64  
 Hirose, S., Krolik, J. H., & Blaes, O. 2009, *ApJ*, 691, 16  
 Jiang, Y.-F., Cantiello, M., Bildsten, L., Quataert, E., & Blaes, O. 2015, *ApJ*, 813, 74  
 —. 2016a, *arXiv:1612.06434*  
 Jiang, Y.-F., Davis, S. W., & Stone, J. M. 2016b, *ApJ*, 827, 10  
 Jiang, Y.-F., Guillochon, J., & Loeb, A. 2016c, *ApJ*, 830, 125  
 Jiang, Y.-F., Stone, J. M., & Davis, S. W. 2012, *ApJS*, 199, 14  
 —. 2013a, *ApJ*, 778, 65  
 —. 2013b, *ApJ*, 767, 148  
 —. 2014a, *ApJ*, 796, 106  
 —. 2014b, *ApJS*, 213, 7  
 —. 2014c, *ApJ*, 784, 169  
 Jin, C., Done, C., & Ward, M. 2016, *MNRAS*, 455, 691  
 —. 2017, *MNRAS*, 468, 3663



- Ju, W., Stone, J. M., & Zhu, Z. 2016, *ApJ*, 823, 81  
—, 2017, [arXiv:1705.00779](https://arxiv.org/abs/1705.00779)
- Kato, Y., Mineshige, S., & Shibata, K. 2004, *ApJ*, 605, 307
- Kaufman, J., & Blaes, O. M. 2016, *MNRAS*, 459, 1790
- Kaufman, J., Blaes, O. M., & Hirose, S. 2017, *MNRAS*, 467, 1734
- Kollmeier, J. A., Onken, C. A., Kochanek, C. S., et al. 2006, *ApJ*, 648, 128
- Komossa, S., Voges, W., Xu, D., et al. 2006, *AJ*, 132, 531
- Kormendy, J., & Ho, L. C. 2013, *ARA&A*, 51, 511
- Kratter, K., & Lodato, G. 2016, *ARA&A*, 54, 271
- Luo, B., Brandt, W. N., Hall, P. B., et al. 2015, *ApJ*, 805, 122
- McKinney, J. C., Tchekhovskoy, A., Sadowski, A., & Narayan, R. 2014, *MNRAS*, 441, 3177
- Mihalas, D., & Mihalas, B. W. 1984, *Foundations of radiation hydrodynamics*, ed. Mihalas, D. & Mihalas, B. W.
- Miller, K. A., & Stone, J. M. 2000, *ApJ*, 534, 398
- Mortlock, D. J., Warren, S. J., Venemans, B. P., et al. 2011, *Nature*, 474, 616
- Ohsuga, K., Mori, M., Nakamoto, T., & Mineshige, S. 2005, *ApJ*, 628, 368
- O'Neill, S. M., Reynolds, C. S., Miller, M. C., & Sorathia, K. A. 2011, *ApJ*, 736, 107
- Paczynski, B., & Wiita, P. J. 1980, *A&A*, 88, 23
- Papaloizou, J. C. B., & Lin, D. N. C. 1995, *ARA&A*, 33, 505
- Penna, R. F., Kulkarni, A., & Narayan, R. 2013, *A&A*, 559, A116
- Pounds, K. A., Done, C., & Osborne, J. P. 1995, *MNRAS*, 277, L5
- Rees, M. J. 1988, *Nature*, 333, 523
- Salvesen, G., Simon, J. B., Armitage, P. J., & Begelman, M. C. 2016, *MNRAS*, 457, 857
- Savonije, G. J., Papaloizou, J. C. B., & Lin, D. N. C. 1994, *MNRAS*, 268, 13
- Sądowski, A., Narayan, R., McKinney, J. C., & Tchekhovskoy, A. 2014, *MNRAS*, 439, 503
- Shakura, N. I., & Sunyaev, R. A. 1973, *A&A*, 24, 337
- Shakura, N. I., Sunyaev, R. A., & Zilitinkevich, S. S. 1978, *A&A*, 62, 179
- Shi, J., Krolik, J. H., & Hirose, S. 2010, *ApJ*, 708, 1716
- Shu, F. H., & Lubow, S. H. 1981, *ARA&A*, 19, 277
- Simon, J. B., Bai, X.-N., Armitage, P. J., Stone, J. M., & Beckwith, K. 2013, *ApJ*, 775, 73
- Simon, J. B., Beckwith, K., & Armitage, P. J. 2012, *MNRAS*, 422, 2685
- Socrates, A., Davis, S. W., & Blaes, O. 2004, *ApJ*, 601, 405
- Sorathia, K. A., Reynolds, C. S., Stone, J. M., & Beckwith, K. 2012, *ApJ*, 749, 189
- Stella, L., & Rosner, R. 1984, *ApJ*, 277, 312
- Stone, J. M., Gardiner, T. A., Teuben, P., Hawley, J. F., & Simon, J. B. 2008, *ApJS*, 178, 137
- Stone, J. M., Hawley, J. F., Gammie, C. F., & Balbus, S. A. 1996, *ApJ*, 463, 656
- Suzuki, T. K., & Inutsuka, S.-i. 2014, *ApJ*, 784, 121
- Turner, N. J. 2004, *ApJ*, 605, L45
- Turner, N. J., Stone, J. M., Krolik, J. H., & Sano, T. 2003, *ApJ*, 593, 992
- Volonteri, M., Silk, J., & Dubus, G. 2015, *ApJ*, 804, 148
- Zhu, Y., & Narayan, R. 2013, *MNRAS*, 434, 2262
- Zhu, Z., & Stone, J. M. 2017, [arXiv:1701.04627](https://arxiv.org/abs/1701.04627)